SEISMIC REFLECTION INVERSION BY BASIS PURSUIT

A Dissertation

Presented to

the Faculty of the Department of Earth and Atmospheric Sciences

University of Houston

In Partial Fulfillment

of the Requirements for the Degree

Doctor of Philosophy

By

Rui Zhang

December 2008

SEISMIC REFLECTION INVERSION BY BASIS PURSUIT

Rui Zhang

APPROVED:

John Castagna, Chairman
Dept. of Earth and Atmospheric Sciences

Christopher Liner
Dept. of Earth and Atmospheric Sciences

Aibing Li
Dept. of Earth and Atmospheric Sciences

Tad Smith
Apache Corporation

Dean, College of Natural Sciences and Mathematics

Acknowledgements

First and foremost, I would like to express my gratitude to my advisor, Dr. John Castagna, for his guidance and wisdom throughout my Ph.D. study and research. Dr. Castagna brought me into a brand new research field and helped me work out an exciting Ph.D research subject. He has always been around for encouragement, assistance and inspiration in many aspects during the past four years. Without his constant support, this dissertation would never have shaped. I would also like to thank Dr. Christopher Liner, Dr. Aibing Li, Dr. Tad Smith for serving on my committee. Their insightful comments provided valuable inputs to my dissertation.

I extend my warmest gratitude to my friends and colleagues at UH: Charles Puryear, Dip Shankar Nanda, Chingwen Chen, Cecilia Ramirez, Ayato Kato, Aslan-Gassiyev V.

Many thanks also go to the donors of multiple financial support sources without which my Ph.D. study and research would have been impossible. They are: G&W Systems grants,UH Department of Earth and Atmospheric Sciences Fellowship, SEG Scholarship and GSH Scholarship.

Finally, I would like to thank my parents for standing behind me all the time.

Abstract

In this dissertation we develop a seismic reflection inversion procedure using a basis pursuit technique, that reconstructs the subsurface microstructure from poststack seismic data. We first explain the formula underlying basis pursuit inversion (BPI) for seismic reflection, before investigating the formula through the incorporation of a priori information.

BPI is a type of L_1 norm constrained least square solution for inverse problems. Compared with the other two kinds of constraints ($L_p, (p = 0, 2)$ norm minimization), minimal L_1 norm constraint is best at recovering an accurate reflectivity series. A minimal L_0 norm constraint can be obtained by use of a matching pursuit (MP) method that produces sparse solutions. A minimal L_2 norm constraint can be obtained by use of general inversion method that produces smooth solutions. The BPI technique balances the sparseness and smoothness to achieve a dense spiky solution.

Specifically, our BPI incorporates wedge models as the basis instead of any impedance starting models. The incorporation is achieved by dipole decomposition, which can decompose any reflector pair into an odd and even pair. By using the formulism, BPI recovers the subsurface structure in the form of reflection coefficients. Synthetic

tests show the sensitivity of BPI, even given the inaccuracy of wavelets and the presence noise contamination. Sparse-spike inversion (SSI) is another minimal L_1 norm constraint least square methods which has been used in industry for decades. A comparison between BPI and SSI suggests the improvement of BPI.

We test BPI with several field data sets: an improved tie between well-log data with the inverted data illustrating the superior vertical resolution from BPI; improved imaging of subtle stratigraphic features with removing the wavelet effect; impact on the 3-D data set interpretation; improved velocity structure. Various data applications show the industrial potential of BPI to be incorporated .

Contents

List of Figures

Chapter 1

Introduction and Motivation

The basic goal in reflection seismology is to recover the layered structure of the surface as a function of depth from observed seismic data. This goal is not easily attained, for even if the convolutional model is adopted and the earth is assumed to be made up of plane parallel layers having constant material parameters. The main difficulty lies in the bandlimited effect of seismic data with the resulting loss of low- and high-frequency information about subsurface structure. The purpose of this dissertation is to invert a high resolution reflection coefficients series from each poststack seismic trace. Since it is the most widely used, the the convolutional model is applied here for poststack seismic images permitting each seismic trace $s(t)$ to be shown in Figure 1.1. This can also expressed as Eq. 1.1:

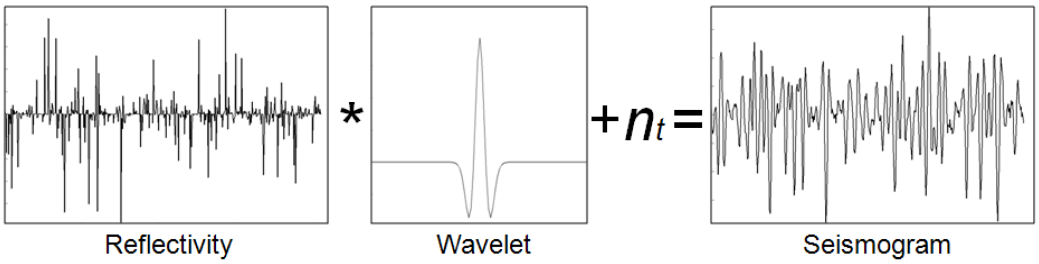

Figure 1.1: Seismic trace as convolution of wavelet with reflectivity

$$s(t) = w(t) * r(t) + n(t) \tag{1.1}$$

where $w(t)$ is the seismic wavelet, $*$ is the convolution operation symbol, $r(t)$ is the unknown reflectivity series and $n(t)$ is random noise. Mathematically, convolution can be written as a formula as shown in Eq. 1.2:

$$s(t) = \int w(t-\tau)r(\tau)d\tau + n(t) \tag{1.2}$$

This model assumes that the earth's structure can be represented adequately by a set of planar layers of constant impedance. All the reflectors are generated at the boundary between adjacent layers. For the purpose of this dissertation, We also assume the wavelet (or an estimate of the wavelet) is known through a constant-phase shift.

It is clear that because of the bandwidth limitation of the wavelet (and data) and because the data are finite and inaccurate, there exists an infinite number of reflectivities that fit the data equally well. These possibilities are the source of non-uniqueness. One reflectivity should be chosen as the *right* one using some criteria or

constraint. So, the *right* solution should: (1) fit the data;(2) satisfy a given set of constraints (if available). The first issue leads to a least-square solution which is a common solution of geophysical inversion problems. The second issue represents the key point to most inverse problems. It is usually put into practice by assuming certain prior information about the type of solution one is interested in finding. In other words, prior information is used to discard implausible models. In this dissertation, three kinds constraint solutions will be studied and the solution with a minimal L_1 norm is shown to be the best for seismic reflection inversion.

In this dissertation we assume that reflectivity is a series of spikes. The main objective of the inversion method is to provide a significant increase in bandwidth content from bandlimited seismic observations. This is especially important because the search for subtle hydrocarbon traps has become a major task in today seismic exploration. Under the assumption of sparseness, the seismic problem involves: (1) detection of the spikes; and (2) estimation of their amplitudes.

Various methods use different search strategies to locate the spikes and rely on the optimization of different cost functions to satisfy a probabilistic model for the reflectivity (**?**; **?**). Other methods proceed to optimize some norm that forces the solution to be sparse (**?**; **?**; **?**; **?**; **?**; **?**). **?** address the problem (through the inversion of post-stack data) using sparse prior information. In their method, numerical instabilities in the linear least-squares stage are handled by introducing constraints in the spike locations; for example, two spikes cannot be closer than a predetermined distance. This precludes the use of the procedure in geologic situations such as layer pinch-outs

and thin beds. Another difficulty mentioned comes from the fact that the linear stage may lead to solutions with invalid amplitudes. Hence, the use of constrained linear optimization is suggested to alleviate this problem, though it is not clearly explained how these constraints are included from a numerical point of view.

? provide a first look at high resolution inversion through a spectral inversion technique that describes the possibility of resolvable thin layers that are less than tuning thickness. Further applications of spectral inversion are presented by ? that yield superior resolution which can help in various ways. The advantages include being able to pick up more reflection detail, to perform more accurate interpretation on seismic volumes obtained by convolving reflectivity volumes with wavelets of higher bandwidth than the input data, and to visualize subtle anomalies when some attributes are run on thin-bed reflectivity inversion outputs. The theory of spectral inversion was refined by ? in detail that demonstrated its utility by performing layer thickness determinations on a real seismic survey (without well calibration) to achieve estimation accuracies of a few milliseconds at time for thicknesses approaching 1/16 of a wavelength. ? also demonstrated how much more geologically reasonable inverted reflectivity images are, from a stratigraphic point of view, than are the seismic sections from which they are derived. The output of the inversion process can be viewed as spectrally broadened seismic data, retrieved in the form of broadband reflectivity data that can be filtered back to any bandwidth that filter panel tests have indicated adds useful information for interpretation purposes.

In contrast to spectral inversion that is a spectral domain method, basis pursuit

inversion (BPI) is applied in time domain. The dissertation proposes that BPI yields stable and valid solutions without the need for explicitly constraining either the location, or the amplitudes of the reflection coefficients and initial model. Furthermore, because the proposed trace-by-trace strategy provides good lateral continuity, the use of additional terms in the cost function is not required.

The proposed methodology in this dissertation allows for any number of spikes to be easily incorporated into the optimization procedure to further reduce the nonuniqueness of the solution and to improve its accuracy and consistency.

In Chapter 2, we compare three kinds of $L_p, p = 1, 2, 3$ norm constraint least-square solutions, showing that the L_1 norm minimization constraint is the best for seismic reflectivity inversion. In Chapter 3 a wedge dictionary is introduced which is shown to have a superior ability to help resolve thin-bed layers. In Chapter 4, we analyze the sensitivity of BPI regarding kernel matrix, wavelet inaccuracies and noise using synthetic tests. Chapter 5 presents field data applications. We present our conclusions in Chapter 6.

Chapter 2

Inversion Theory

In this chapter, we will discuss the general inversion theory. Three kinds of L_p norm constraint least-square methods are presented and compared.

2.1 Convolution Model

In this dissertation, the subsurface is considered to have the structure of layer cake. Each layer consists of uniform properties and each interface between two layers generates reflection. Poststack seismic data gives an image of the earth that describes the spatial distribution of those interfaces. Each trace of poststack seismic image can be considered as a convolution of a seismic wavelet with the reflectivity series as was stated in Eq. 1.1. Mathematically, the convolution operation is integration, as was shown in Eq. 1.2. Reflectivity here is considered as a normal incident.

It is known that the convolution integration can be transformed into the multiplication of a reflectivity vector with a kernel matrix. Figure 2.1 illustrates the simple

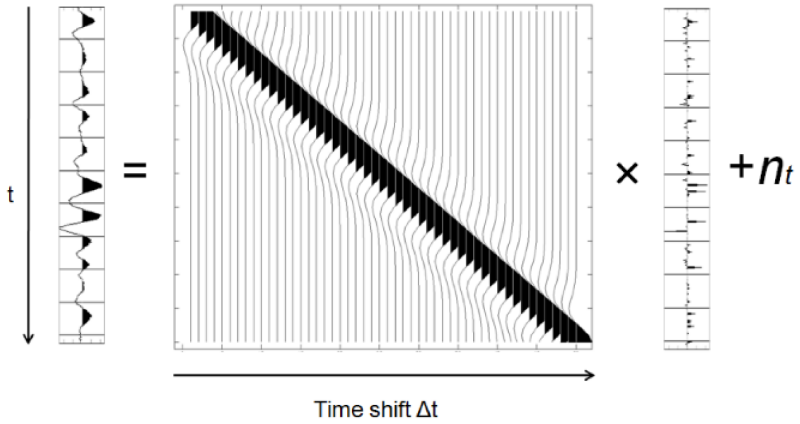

Figure 2.1: The matrix form of convolution

convolutional operation using matrix multiplication. The kernel matrix is a diagonal matrix with the wavelet shifting from start to the end. So, the convolution model can be written as Eq. 2.1.

$$d = Gm + n, \tag{2.1}$$

Where the d represents the seismogram data $s(t)$ in the Eq. 1.1; m represents the $r(t)$ and **G** represents the diagonal wavelet matrix. n is assumed to be a random noise, making the least-square solution possible. The least-square solution minimizes the means square error between the forward modeling and observed data which suffers from the nonuniqueness. To solve the nonuniqueness, a constraint has to be induced to choose the "right" solution from all the possibilities.

2.2 L_p Norm Constraint

Seismic reflection inversion commits itself to removing the effects of a *blurring* kernel-wavelet matrix- on the seismic image. The blurring kernel, known as the seismic wavelet, contains the effects of the source-function. The model ,m, represents

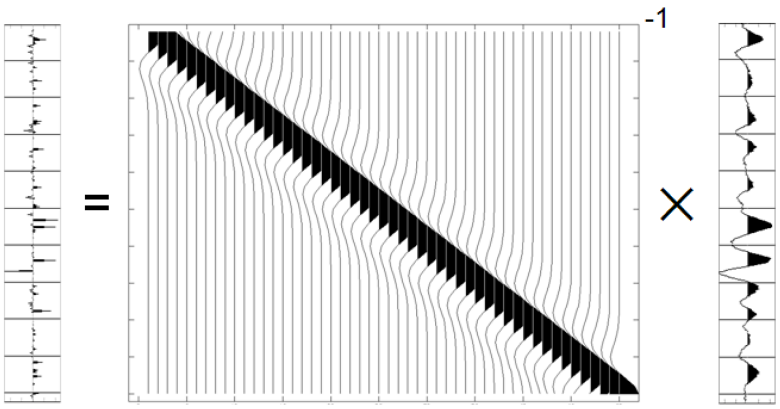

Figure 2.2: Reflectivity can calculated by multiplying inverse wavelet matrix with seismic trace.

the reflectivity (as $r(t)$ in Eq. 1.1) and is linearly related to the observed seismic image trace, d (as $s(t)$ in Eq. 1.1), by the kernel **G**-diagonal wavelet matrix (as $w(t)$ in Eq. 1.1). n is taken to be a white Gaussian noise. With a slight abuse of notation, we will replace the operator, model and data by a matrix and vectors. The reflection coefficients vector m is designed to be sparse; the question is how to find these sparse solution with given (noisy) data. The direct answer would be calculated as shown in Figure 2.2. The may also be represented as Eq. 2.2.

$$m = G^{-1} * d \tag{2.2}$$

Figure 2.3 shows an example of kernel matrix **G** that is constructed with a 30 Hz ricker wavelet shifting from zero to 0.5 s (shown at left) with a direct inverse matrix calculated (shown at right). To characterize the inverse **G** matrix, the eigne values of the inverse **G** matrix are calculated and plotted from large to small in Figure 2.4. It may be observed that the first three largest eigne values are about 4.5×10^{13}, much larger than all the rest. Figure 2.4 (b), the detailed figure within the dashed red

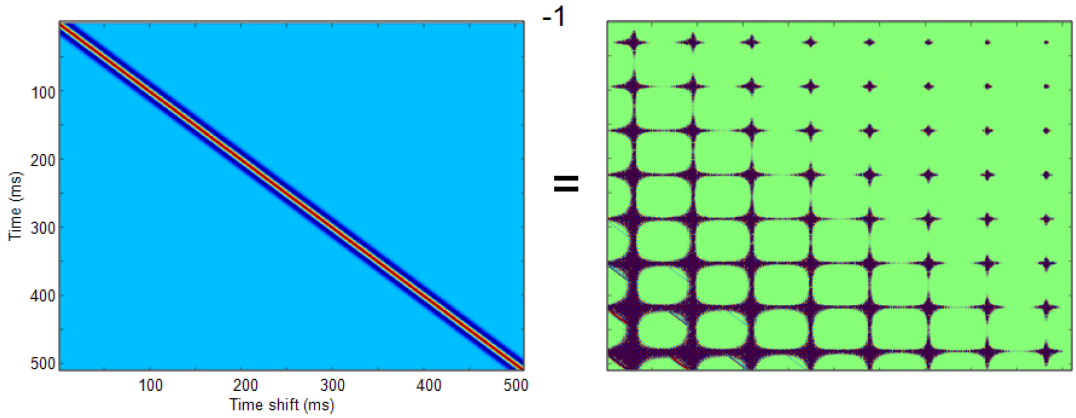

Figure 2.3: Inverse **G** matrix

rectangle, demonstrates that the 4th to about 340th eigne values hold the quantity of about 10^7. The remaining eigne values have a quantity level of 1. Such a big difference in eigen value means that the inverse **G** matrix is very *ill*. An ill-posed inverse problem usually leads to instable solutions which are very noise sensitive or possess great nonuniqueness.

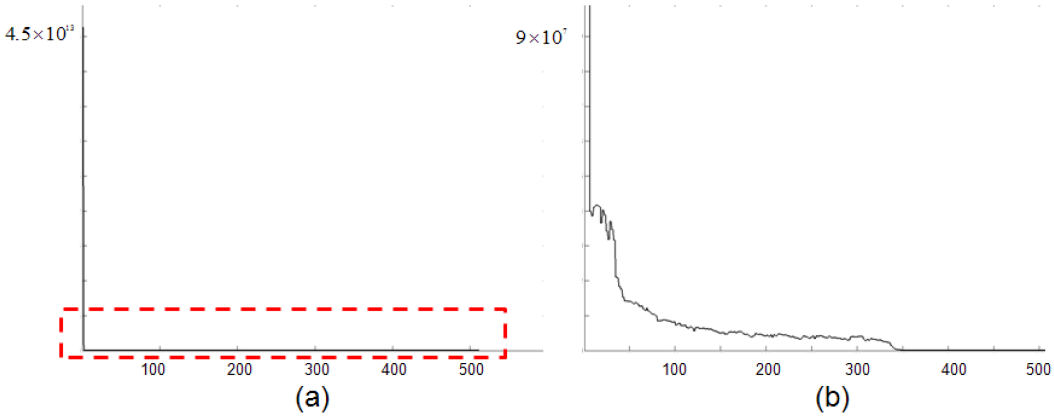

Figure 2.4: Eigne value of inverse **G**

Given the *illness* of **G**, the simple least square solutions could (as shown in Eq.

2.2 and Figure 2.2) can have the problems below:

· non-uniqueness;

· unstable;

· lack of resolution;

· inferior denoising capabilities.

Suffering from above weaknesses, least-square solutions have to be constrained to the one providing the best fit to reality. Such a constraint is usually described as in Eq. 2.3

$$\min \|d - Gm\|_2 + \lambda J(m), \tag{2.3}$$

where $J(m)$ is a λ-weighted global constraint function (**?**), which contains a *priori* information on the model. The constraint term $J(m)$ works from the model; it is usually a function of model parameters. λ, the trade-off factor, plays an important role in the inversion processing that balances the mean square error with a penalty function to derive the best result. This formulation underlines many least-square inversion techniques and permits a reflectivity model (**?**, **?**).

Currently, L_0, L_1 and L_2 norms are three kinds of commonly used constraint functions. The L_2 norm constraint is more widely used in inversions with a target having a smooth distribution, such as the velocity model, because it has a tendency to spread the energy. The L_1 and L_0 norms, on the other hand, preserve sparseness. Such sparseness-constrained inversion techniques (**?**,**?**) can produce successful spikes train solutions of the inverse problem. In this dissertation, the earth is supposed to consist of isolated jump discontinuities - a reflectivity series. I will discuss $p = 0$, $p = 2$ and $p = 1$, respectively.

$p = 0$: leads to Matching Pursuit (MP). MP minimizes the number of non-zero coefficients by applying a simple recursive rule that selects the best matching atoms with a greedy search strategy (**?**). When it is applied in a time-frequency decomposition with some orthogonal or biorthogonal time-frequency atoms, it becomes a spectral decomposition. MP can also be adopted in seismic reflection inversion by replacing time-frequency atoms by a seismic wavelet, as shown below:

$$min\|d - Gm\|_2^2 + \lambda\|m\|_0, \tag{2.4}$$

$p = 2$: leads to a L_2 norm minimization constrained least square solution. When it is applied in velocity inversion, it becomes tomography. When it is applied in a seismic reflection inversion, it becomes similar to a deconvolution, as shown below;

$$min\|d - Gm\|_2^2 + \lambda\|m\|_2, \tag{2.5}$$

$p = 1$: leads to a sparseness-constraint global optimization scheme. There are different types of algorithms to realize the L_1 norm minimization. Each has the same expression shown below:

$$min\|d - Gm\|_2^2 + \lambda\|m\|_1, \tag{2.6}$$

We will compare three different strategies to obtain a reflectivity series, with emphasis on the seismic application and the selection of a reflection coefficient vector. While deconvolution and basis pursuit methods are based on solving a global optimization problem, the MP method uses a *local* greedy search algorithm (**?**). **?** has

discussed the three kinds of methods, with an application of time frequency decomposition, in detail. We compare these three kinds of method with applications in seismic reflection inversion respectively.

2.3 Basis Pursuit

Original basis pursuit was developed as optimization method. It finds signal representations in overcomplete dictionaries by convex optimization. It obtains the decomposition with a minimal L_1 norm of the corresponding coefficients occurring in the representation. Because of the non-differentiability of the L_1 norm, this optimization principle leads to decompositions that can have very different properties from the sparse representation methods; in particular, they can be much sparser. Because it is based on global optimization, it can stably super-resolve in ways that Matching Pursuit (MP) cannot.

When the basis pursuit technique is applied in a seismic reflection inversion, each seismic image trace (d in Eq. 2.1) is a discrete time signal of length n-time samples, with a recording sample rate; this may also be viewed as a n-dimension vector. Seismic reflection inversion can be considered as the reconstruction of this signal with superpositions of seismic response ($\mathbf{G}$ in Eq. 2.1) with specific coefficients–reflection coefficients (m in Eq. 2.1).

2.3.1 Linear Program

The application of BPI in seismic reflection inversion is to find a representation of the seismic image trace whose coefficients have a minimal L_1 norm. The expression (shown in Eq. 2.6) only gives some mathematic meaning of BPI that is not explicitly resolvable. The realization of a solution of the BPI has been described in detail by **?**. BPI can be equivalently reformulated as a linear program by making the following translations:

$$m = u - v; x = \begin{pmatrix} u \\ \\ v \end{pmatrix}; A = (G, -G); b = d; c = \lambda(1, 1). \tag{2.7}$$

By these transformations, minimal r can be transformed into minimization of the new positive variable x, because

$$\|r\|_1 = \|u - v\|_1 \leq \|u\|_1 + \|v\|_1 = x. \tag{2.8}$$

The Eq. 2.1 then can be changed into Equation as $Ax = b$. So the explicitly resolvable equation can be changed into a constraint optimization problem as

$$\min c^T x \qquad subject \qquad to \qquad Ax = b, \qquad x \geq 0 \tag{2.9}$$

This expression is what Sparse-Spike Inversion (SSI) is solving. Different from SSI, BPI utilizes a Primal-Dual method. It solves *primal*, *dual* and *gap* equations simultaneously.

2.3.2 Duality Theory

Eq. 2.9 is often called the primal linear program. The primal linear program is equivalent to the dual linear program:

$$\max b^T y \qquad subject \qquad to \qquad A^T y + z = c, z \geq 0, \tag{2.10}$$

where x is called the primal variable; and y and z are called the dual variables. The term *primal infeasibility* refers to the quantity $\|b - Ax\|_2$; the term *dual infeasibility* refers to $\|c - z - A^T y\|$; the term *duality gap* refers to the difference between the primal objective and the dual objective: $c^T x - b^T y$. BPI solves these equations – *primal*, *dual* and *gap* equations simultaneously.

A fundamental theorem of linear programming states that (x, y, z) solves the linear program (Eq. 2.9), if and only if the primal infeasibility, the dual infeasibility and the duality gap are all zero. Therefore, when (x, y, z) are nearly primal feasible and nearly dual feasible, the duality gap offers a good description about the accuracy of (x, y, z) as a solution: the smaller the duality gap is, the closer (x, y, z) are to the optimal solution.

Our approach is based on a primal-dual log-barrier algorithm. In order to regularize above Eq. 2.9 and 2.10, **?** proposed solving the following perturbed Linear Program:

$$\max c^T x + \frac{1}{2}\|\gamma x\|^2 + \frac{1}{2}\|p\|^2 \qquad subject \qquad to \qquad Ax + \delta y = b, x \geq 0. \tag{2.11}$$

2.3.3 A Primal-Dual log-Barrier LP Algorithm

The main steps of the primal-dual log-barrier algorithm are as follows:

1. Set parameters: the feasibility tolerance $FeaTol$, the duality gap tolerance $PDGapTol$, the two regularization parameters γ and δ .

2. Initialize $x > 0$, $y, z > 0$, $\mu > 0$. Set $k = 0$.

3. Loop

(a) set:

$$\begin{aligned} t &= c + \gamma^2 x - z - A^T y \\ r &= b - Ax - \delta^2 y \\ v &= \mu e - Zx \\ D &= (X^{-1}Z + \gamma^2 I)^{-1} \end{aligned} \tag{2.12}$$

where X and Z are diagonal matrices composed from x and z; e is a vector of ones;

(b) solve:

$$(ADA^T + \delta^2 I)\Delta y = r - AD(X^{-1}v - t) \tag{2.13}$$

for Δy and set

$$\Delta x = DA^T \Delta y + D(X^{-1}v - t), \Delta z = X^{-1}v - X^{-1}Z\Delta x; \tag{2.14}$$

(c) Calculate the primal and dual step sizes ρ_p,ρ_d and update the variables:

$$\begin{aligned} \rho_p &= 0.99 \times \max \rho : x + \rho \Delta x \geq 0, \\ \rho_d &= 0.99 \times \max \rho : z + \rho \Delta z \geq 0; \\ x &= x + \rho_p \Delta x, \\ y &= y + \rho_d \Delta y, \\ z &= z + \rho_d \Delta z, \\ \mu &= (1 - \min(\rho_p, \rho_d, 0.99))\mu. \end{aligned} \tag{2.15}$$

4. Terminate if the following three conditions are satisfied:

(a) Primal infeasibility= $\frac{\|r\|_2}{1+\|x\|_2}$ <FeaTol;

(b) Dual infeasibility= $\frac{\|t\|_2}{1+\|y\|_2}$ <FeaTol;

(c) Duality gap= $\frac{z^T x}{1+\|z\|_2\|x\|_2}$ <PDGapTol;

For fuller discussions of this and related algorithms, see (**?**, **?**, **?**, **?**,**?**). Note that when $\delta > 0$, the central Eq. 2.13 may be written as the least-square problem:

$$\min_{\Delta y} \left\| \begin{pmatrix} D^{1/2} A^T \\ \delta I \end{pmatrix} \Delta y - \begin{pmatrix} D^{1/2}(t - X_{-1} v) \\ r/\delta \end{pmatrix} \right\|_2, \tag{2.16}$$

which may be better suited to a numerical solution if δ is not too small. While in principle we could have based our approach on other interior-point schemes, the primal-dual approach naturally incorporates several features we found useful. First,

the iterates x, y, z do not have to be feasible. We are only able to choose a starting point that is *nearly* feasible and remain *nearly* feasible throughout the sequence of iterations. Second, after both primal and dual feasibility have been nearly achieved, it is easy to check for closeness to the solution value; at the limiting solution $c^T x^* = b^T y^*$ and the duality gap $c^T x - b^T y \approx x^T z$ quantify the distance from this ideal.

The bottleneck in the linear approaches presented in the BPI is that the methods either suffer from sensitivities, when the waveforms "interfere" yielding waveforms that are not present in the dictionary, or from the inability of the L_1 norm to impose sparseness for a highly redundant dictionary with waveforms that are relatively close in their behavior and potential to amplify the noise. In that sense, our problem turns out to be similar to many (geophysical) inversion problems plagued by nonuniqueness. The balance between sensitivities and redundancies of the dictionary is pursued by varying the tradeoff factor λ. Another issue for our BPI is the computation time. Because our BPI solution utilizes the Newton-Gaussian step method, it is more time consuming than the other two methods. Nonetheless, processing speeds are increasing quickly and parallel computation techniques are becoming more and more powerful. Computation speed will not be the problem.

2.4 Matching Pursuit

? have presented a theoretical basis for Matching Pursuit (MP) mainly in the application of time-frequency decomposition. Time-frequency decomposition relies heavily on the orthogonality or biorthogonality of time-frequency atoms, which are

not satisfied in seismic inversion. **?** adopts a MP algorithm in a seismic reflection inversion in his dissertation by formulating the inversion problem as Eq. 2.17:

$$s = \Sigma_{n=0}^{m-1} r_n W_n + R^m s, \tag{2.17}$$

where s is the seismic image trace; r_n is the nonzero reflection coefficient; W_n is the seismic response element, which can be considered as each column of the $\mathbf{G}$ matrix; and R^n represents the residual after m iteration. Starting from an initial approximation $s_0 = 0$ and residual $R^0 = s$, the method builds up a sequence of sparse approximations stepwise. At stage m, it identifies the dictionary atom that best correlates with the residual, then adds to the current approximation a scalar multiple of that atom, so that $s_k = s_{k-1} + r_k W_k$, where $r_k =< R^{k-1}s, W_k >$ and residue $R^k s = s - s_k$. After k steps, one has a representation of Eq. 2.17, where the original signal is decomposed into a series of dictionary elements with corresponding coefficients and the residual $R = R^k$. An intrinsic feature of the algorithm is that when stopped after a few steps, it yields an approximation using only a few atoms. Because the most common application of Matching Pursuit is in a time frequency decomposition, it utilizes a family of orthogonal time-frequency atoms. When the dictionary is orthogonal, the method works perfectly. If the object is made up of only $m < n$ atoms, and the algorithm is run for m steps, it recovers the underlying sparse structure exactly.

When applied in a seismic reflection inversion, MP utilizes a seismic wavelet instead of any orthogonal or biorthogonal time-frequency atoms. Such a wavelet is

usually derived from the seismic data. When the dictionary is not orthogonal, the situation is less clear. Because the algorithm is myopic, one expects that, in certain cases, it might choose incorrectly in the first few iterations and, in such cases, end up spending most of its time correcting for any mistakes made in the first few terms. In fact ,this does seem to happen in practice.

The implementation of MP in a seismic inversion differs from time-frequency decomposition applications only in the construction of the elements dictionary. The dictionary for a seismic reflection inversion consists of the seismic response of the corresponding wavelet and reflectivity patterns. For example, any reflection series can be represented as the summation of a series of isolated spikes with corresponding coefficients. The isolated spike and its corresponding seismic response are shown in Eq. 2.18:

$$W_{t_i} = w(t) * \delta(t - \tau_i), \tag{2.18}$$

where $w(t)$ is the seismic wavelet; τ_i represents the time shift; and W_{t_i} is the seismic response. So any seismic image trace $s(t)$, combining with Eq. 2.18, can be described as:

$$s(t) = \sum_{n=-\infty}^{\infty} r_n W_{t_n}(t) + n(t), \tag{2.19}$$

MP chooses the most correlated element ϕ_{t_i} at each iteration from the dictionary, with residual decaying to an acceptable level. The corresponding coefficient – reflection coefficient – is calculated by an inner production of the elements with a seismic image trace as shown in Eq. 2.20:

$$r_i =< s(t), W_{t_i} > . \tag{2.20}$$

So far, MP is going to choose a set of elements $W_{t_i(\tau,t)}, i = 1...M$ that most matches the seismic image trace $s(t)$ at specific time shift t_i. This is done by successive approximations of $s(t)$ with projections on the selected elements from the dictionary. After M step MP processing, the r_i and corresponding element ϕ_{t_i} have been calculated with the acceptable mean square error $R^M s$ left. The final calculated reflectivity series are a summation of the reflection coefficients, as shown in Eq. 2.21:

$$r'(t) = \sum_{i=1}^{M} r_i \delta(t - t_i). \tag{2.21}$$

MP inversion only chooses those most correlated seismic responses with a seismic image trace and optimizes the coefficients on those selected elements. Such a procedure only chases the local optimization at each iteration.

2.5 L_2 Norm Constraint

The L_2 norm minimization constraint, stated as Eq. 2.5, chooses the solution of the minimal L_2 norm. It is mostly common used in tomography because velocity structure is assumed to be smooth; L_2 norm minimization preserves smoothness very well. When it is applied in a seismic reflection inversion, it is similar to the common deconvolution procedure. The difference lies in the kernel $\mathbf{G}$ matrix. Decovolution uses a inverse filter derived only from seismic image data, but a seismic reflection inversion use a well log calibrated wavelet. Detail of this method can be found in many sources, among them (?, ?, ?).

The L_2 norm constraint solution uses Backus-Gilbert (BG) model, which was

first introduced by earthquake seismologists. The detail were discussed in a series of papers: (? ? ?). ? firstly introduced this method into the acoustic impedance inversion. ? summarize the BG solution as used in exploration seismology. The solution is shown as Eq. 2.22:

$$m = G^T \times (G \times G^T + \varepsilon I)^{-1} d, \tag{2.22}$$

where ε plays the same role as trade-off factor λ. Besides tomography and deconvolution, model based acoustic impedance also utilizes an L_2 minimization constraint. The difference between these applications are the definitions of d, m and $\mathbf{G}$ matrix.

2.6 Comparison

To compare the different methods of inversion, a 20 Hz ricker wavelet (shown in the Figure 2.5) is used to generate a 1-D synthetic seismogram. A synthetic reflectivity series has been generated in Figure 2.6 (a) which models the layer cake earth. Its broad band frequency spectrum is shown in Figure 2.7 (a) as much broader than wavelet bandwidth. So, the synthetic seismogram (as shown in Figure 2.6 (b)) is the convolution result of the wavelet and reflectivity calculated from Eq. 1.1, which has similar frequency spectrum shape as a wavelet (shown in Figure 2.7 (b)). The broad band reflectivity series has been filtered by the seismic wavelet into the similar spectral shape as a wavelet, which leads to the band-limited effect. The gaussian noise has been added into the seismogram with an S/N ratio of ten. The comparison of the three kinds constrained inversion methods is compared below in Figure 2.5:

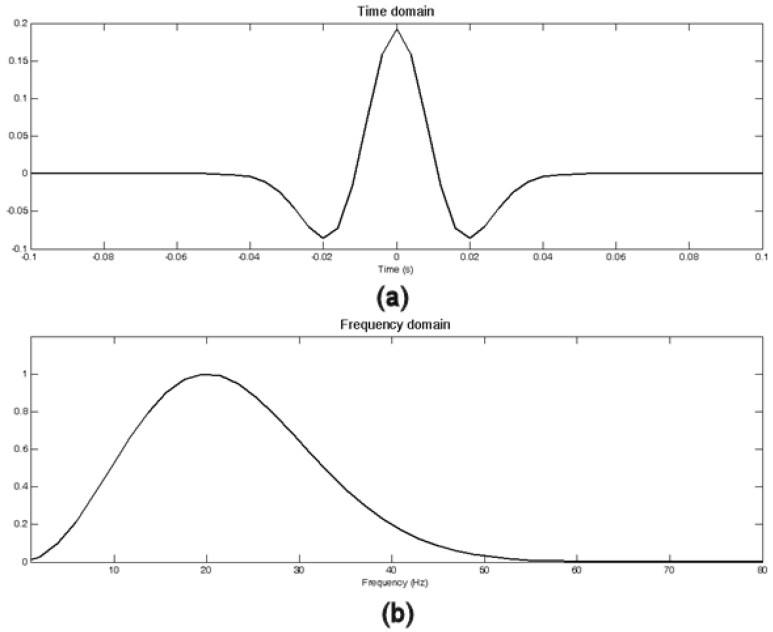

Figure 2.5: Ricker wavelet; (a) time domain; (b) frequency spectrum

Figure 2.6 (c) shows the MP inversion result with a sparse reflectors distribution. The MP solution recovers those most significant events, but loses most minor reflectors because it maximizes the sparseness by minimizing the L_0 norm of the reflectivity series. However those minor reflectors probably relate to a thin bed reservoir. Its broad bandwidth, as shown in the Figure 2.7 (c) comes from the spikes reflectors.

The L_2 norm minimization constraint inversion results are shown in Figure 2.6 (e) and 2.7 (e). As described in previous section, L_2 norm minimization inversion plays as an inverse filter that probably blows up noise. The noise suppression and resolution are balanced by varying the ε to achieve the best result. The results shown here are the best results yielded by changing the ε. In the time domain, a smooth series is shown that is very similar to the deconvolution result. The frequency spectrum

appears as a bandwidth little somewhat broader than that of the wavelet, but still suffering from wavelet effect.

Figure 2.6 (d) and 2.7 (d) show BPI results in time and frequency domains respectively. BPI generates highly dense spikes that maintain the best consistency with true reflectivity as in Figure 2.6 (a) and 2.7 (a). The apparent advantage of the BP inversion comes from the L_1 norm minimization that balances the sparseness of the L_0

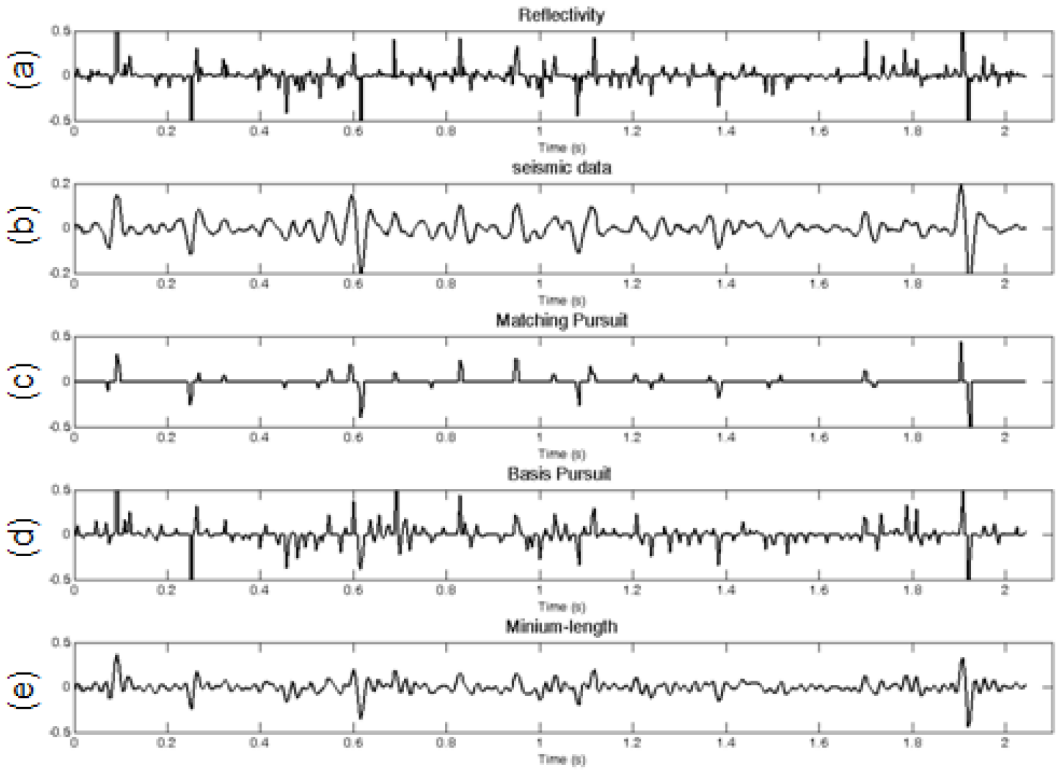

Figure 2.6: Time domain synthetic, (a) true reflectivity; (b) synthetic seismogram; (c) MP inversion result; (d) BP inversion result; (e) deconvolution result.

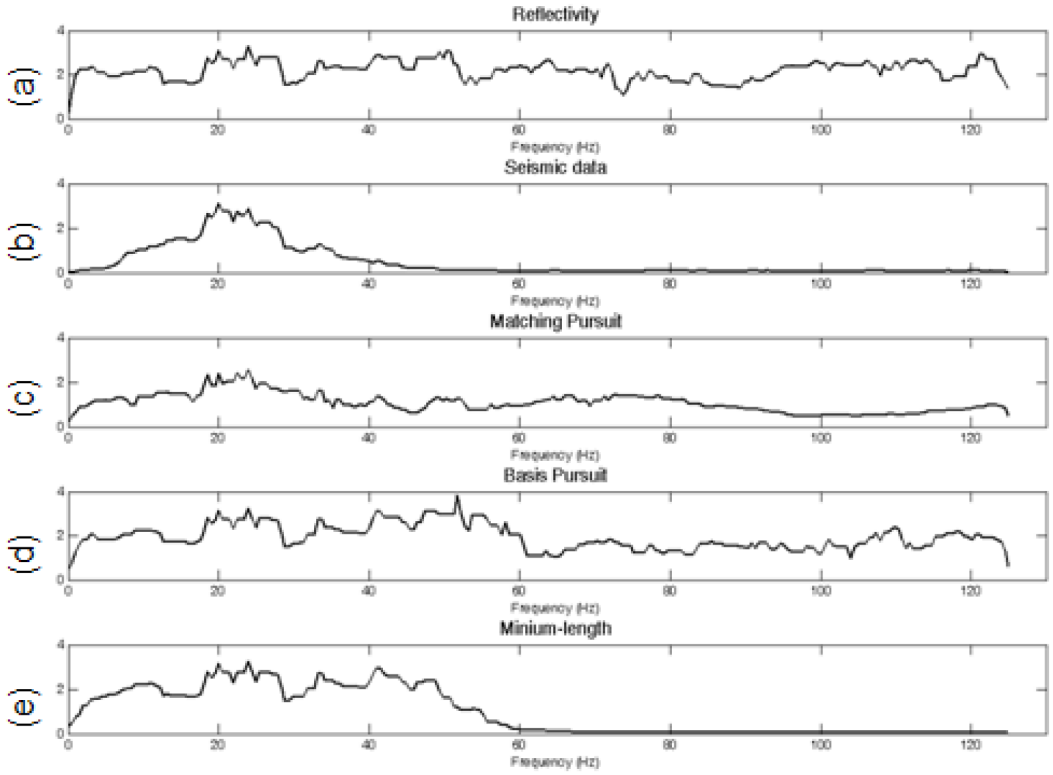

Figure 2.7: Frequency domain synthetic, (a) true reflectivity; (b) synthetic seismogram; (c) MP inversion result; (d) BP inversion result; (e) deconvolution result.

Chapter 3

Wedge Dictionary

In the previous chapter, the basis pursuit inversion (BPI) was shown to have an advantage for seismic reflection inversions. However, even superior resolution has become more and more necessary for oil field development to detect thin bed reservoirs. Thin bed layers usually generate a pair of reflectors at the top and bottom which become thin bed reflectors. Because thin bed layers have a very small bed thickness, the reflector pairs are very close to each other (with time interval $\delta t < 1/4T$, where T is the period of the wavelet) and their seismic responses will interfere with each other (**?**). This interference becomes the main difficulty in resolving the thin bed, which has been considered to be a limitation for seismic resolution. To *resolve* such thin bed reflectors, we will use a wedge dictionary leading to a much higher resolution than using conventional methods.

3.1 Dipole Decomposition

Because thin bed reflectors can be considered as a reflector pair, which can be represented as two impulse functions $c\delta(t)$ and $d\delta(t+\Delta t)$, where Δt is time thickness of the thin bed, c and d are two reflection coefficients. Dipole decomposition will decompose any reflector pair into one even pair r_e and one odd pair r_o, as shown in Eq. 3.1:

$$r_e = \delta(t) + \delta(t+\Delta t); r_o = \delta(t) - \delta(t+\Delta t), \tag{3.1}$$

The corresponding coefficients a and b, as shown in Figure 3.1, can be expressed as in Eq. 3.2:

$$c\delta(t) + d\delta(t+\Delta t) = ar_e + br_o, \tag{3.2}$$

The decomposition coefficients are unique.

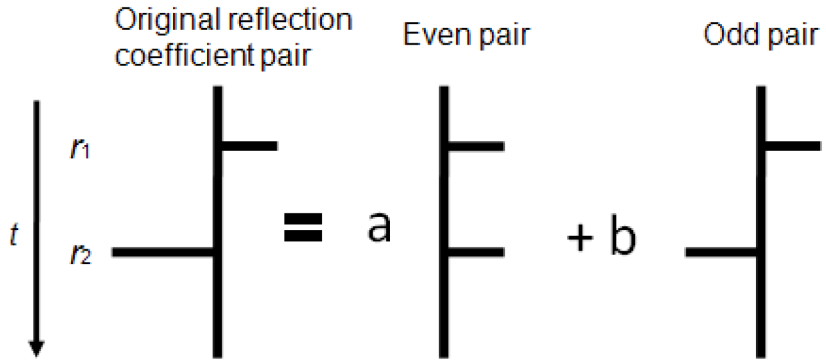

Figure 3.1: Any reflector pair can be considered as summation of one even and odd pair

Unfortunately, the thin bed thickness Δt is usually unknown in practice. To cover all possible bed thicknesses, a complete dipoles model is constructed, leading to a wedge dictionary.

3.2 Wedge Dictionary

The wedge model is a collection of dipole reflectors with the interval increasing from zero to a specific interval, as shown in the Figure 3.2. Figure 3.2 (a) and (b) are even and odd dipole, respectively. Figure 3.2 (c) and (d) are the corresponding seismic response of the even and odd wedge with a given wavelet.

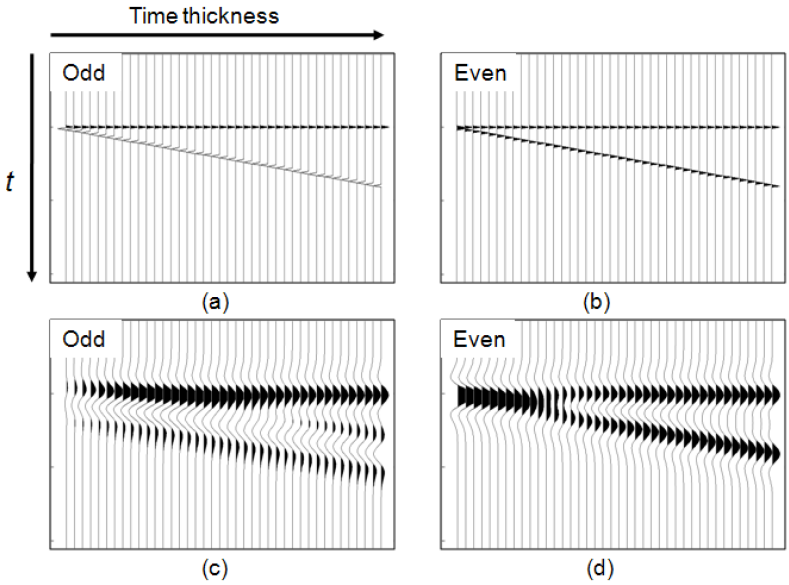

Figure 3.2: Even and odd wedge model and their seismic responses

Suppose the sample rate is Δt. Each trace of the even wedge holds a pair of spikes with an interval of $n\Delta t$, with n increasing from zero to a specific integer. The spikes pair shifts with time scale $m\Delta t$, as m ranges from the first sample to the last one. So, each even wedge reflectivity can be written as:

$$r_e(t, m, n, \Delta t) = \delta(t - m\Delta t) + \delta(t - m\Delta t + n\Delta t) \tag{3.3}$$

The odd wedge has the same pattern as the even wedge, except that the dipoles are

opposite:

$$r_o(t, m, n, \Delta t) = \delta(t - m\Delta t) - \delta(t - m\Delta t + n\Delta t) \tag{3.4}$$

So, any reflectivity series can be considered as a summation of even and odd wedges with a time shift along the time axis, as shown in Eq. 3.5:

$$r(t) = \sum_{n=1}^{N} \sum_{m=1}^{M} (a_{n,m} * r_e(t, m, n, \Delta t) + b_{n,m} * r_e(t, m, n, \Delta t)). \tag{3.5}$$

Figure 3.3 shows an example of the reflectivity of 100 samples. Through dipole decomposition, the first piece of summation consists of a dipole with an interval of 1 sample rates that shifts from time zero to time end, summing up with coefficients from $a_{1,1}$ to $a_{1,99}$. The second piece of summation consists of a dipole with an interval of 2 sample rates that shifts from time zero to time end summing up with coefficients from $a_{2,1}$ to $a_{2,98}$. This process continues to the interval of 10 sample rates in this example. The total summation has same pattern for both even and odd wedges; the total number of elements in a summation is listed in Figure 3.3. When convolved with a given wavelet on both sides of Figure 3.3, it gives a similar decomposition of seismic response. On one side, any seismic image trace is the convolutional result of reflectivity with the given wavelet; on the other side, the summation of the seismic response of the wedge model leads to the same seismic image trace. The decomposition of reflectivity into wedge reflectors and the seismic image trace into a wedge seismic response share exactly the same coefficients $a_{n,m}$ and $b_{n,m}$ as shown in Figure 3.4. The problem remains of how to calculate those coefficients $a_{n,m}$ and $b_{n,m}$.

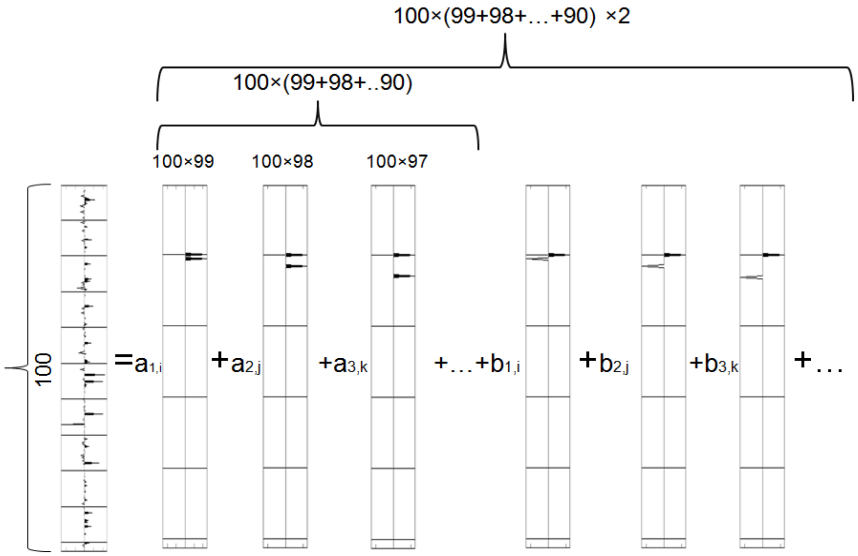

Figure 3.3: Any reflectivity series can be considered as a summation of even and odd wedge

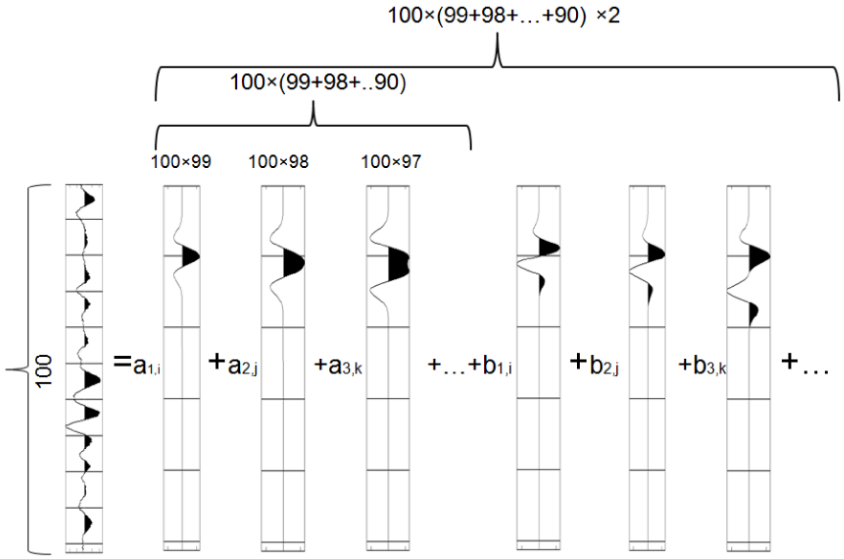

Figure 3.4: Any seismic trace can be considered as a summation of wedge model seismic responses

3.3 Linear Program

To calculate the coefficients $a_{n,m}$ and $b_{n,m}$, Basis Pursuit technique may be applied. Coefficients $a_{n,m}$ and $b_{n,m}$ are first calculated by solving the linear equation (shown in Figure 3.5) with basis pursuit. Using this method, each seismic image trace is decomposed into dipole seismic response elements with the corresponding coefficients $a_{n,m}$ and $b_{n,m}$.

After all of these coefficients are found by basis pursuit (shown in Figure 3.5), the final reflectivity can be calculated by multiplying the above coefficients and the corresponding wedge reflector matrix, as shown in Figure 3.6.

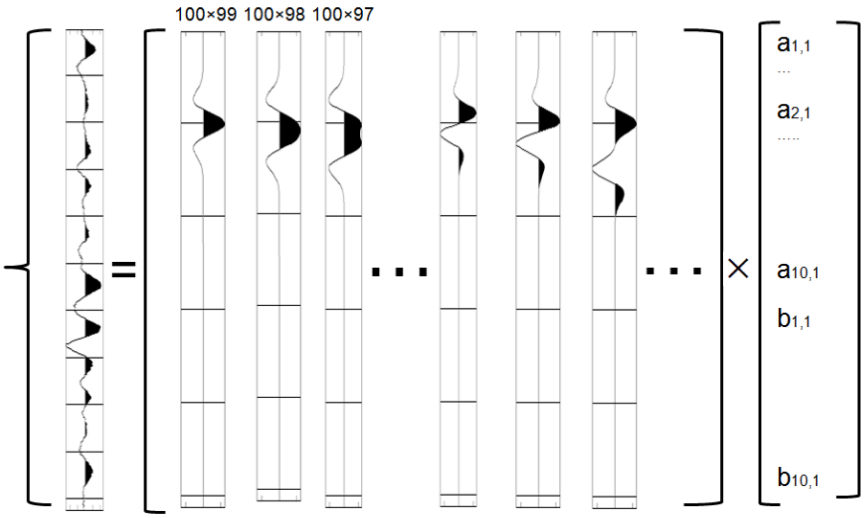

Figure 3.5: Seismic trace as multiplication of dipole seismic response and corresponding coefficients

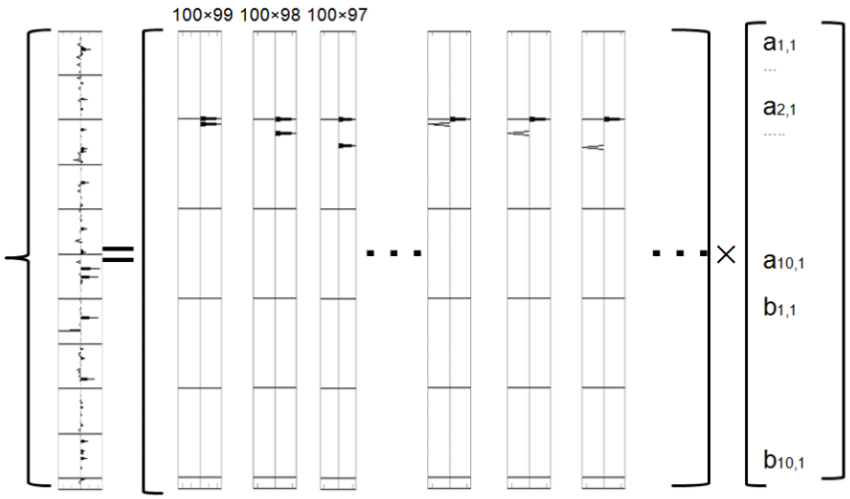

Figure 3.6: Reflectivity can be calculated by multiplying the coefficients $a_{m,n}$ and $b_{m,n}$ with wedge reflectivity.

Chapter 4

Sensitivity Study of BPI

This chapter investigates the sensitivity properties of the BPI algorithm. First, we analyze the effect of wavelet inaccuracy on the BPI because the exact wavelet is never known. Second, we evaluate the sensitivity of BPI to the random noise because seismic data is contaminated with noise. Finally, we compare BPI and SSI inversions demonstrating the uplift of BPI.

4.1 Sensitivity of Inaccurate Wavelets

A poststack seismic image trace is known to be nonstationary with time variant frequency and phase. In practice, it is very hard to utilize a time varying kernel wavelet in any inversion program. Either a simple time varying kernel wavelet may not fit the whole dataset, or such a trend could destabilize the whole inversion program. Usually, a time invariant kernel wavelet, which can be derived from the seismic well tie. Because such a wavelet is usually calculated within a time window which

probably relates to the target zone, it can also be considered as a kernel Jacobin function of seismic image data over well log reflectivity. The seismic image trace within the time window can also be considered as piecewise stationary. We first study the wavelet frequency with synthetic test.

Figure 4.1 shows 30 Hz, 40 Hz and 50 Hz ricker wavelets.

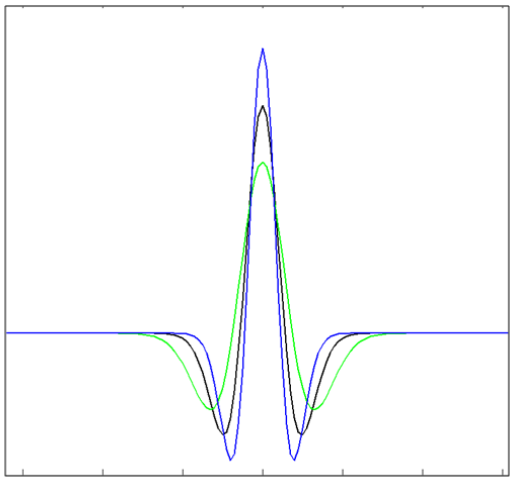

Figure 4.1: Blue is a 50 Hz ricker wavelet; black is a 40 Hz ricker wavelet; green is a 30 Hz ricker wavelet

The 40 Hz ricker wavelet is used to generate a synthetic seismogram with a random reflectivity series (as shown in Figure 4.2 (a) and (b)). All three frequency wavelets are used in BPI respectively. The inverted reflectivity are shown in the Figure 4.2 (c), (d) and (e). As expected, Figure 4.2 (c) shows a good fit inversion result with 40 Hz wavelet. Figure 4.2 (d) shows an inversion result with 30 Hz wavelet showing big biasing from the true reflectivity. 50 Hz wavelet inversion result (shown in Figure 4.2 (e)) shows a spiky result which looks better than than 30 Hz result. The synthetic test shows that an underestimated frequency wavelet might produce a worse inversion

result than an overestimated frequency wavelet. From this test, it appears necessary to have a frequency fit kernel wavelet for our inversion.

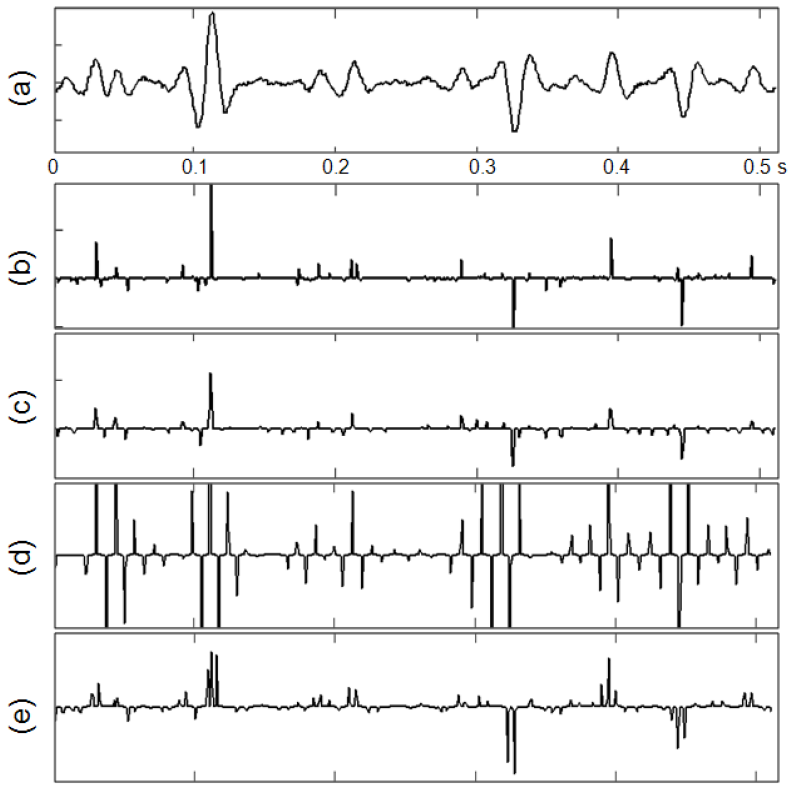

Figure 4.2: (a) shows the synthetic seismogram generated from a 40 Hz ricker wavelet with 10% random noise; (b) true reflectivity; (c) inversion reflectivity with a 40 Hz ricker wavelet; (d) inversion reflectivity with a 30 Hz ricker wavelet; (e) inversion reflectivity with a 50 Hz ricker wavelet.

Besides frequency, phase is also a time variant for any kind of seismic data. It is also very hard to apply a phase change kernel wavelet on an inversion. For simplicity, a constant phase wavelet– minimum phase – is used for inversion. We use a synthetic test to observe the sensitivity of BPI on a wavelet phase.

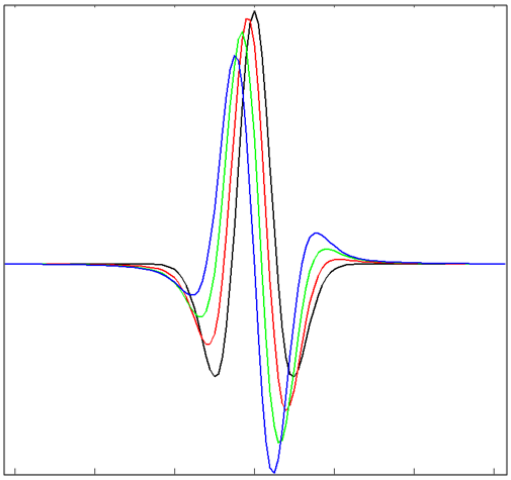

Figure 4.3: Black shows a zero phase ricker wavelet; red is a 30 degree phase rotation; green is a 60 degree phase rotation; blue is a 90 degree phase rotation

Figure 4.3 shows the zero, 30, 60 and 90 degree phase ricker wavelets used for the synthetic test. The zero phase wavelet is used to generate a synthetic seismogram, as shown in Figure 4.4 (a) and (b). Figure 4.4 (c) shows the inversion result with the zero phase wavelet; (d), (e) and (f) show the inversion results with 30, 45 and 90 degree wavelets. Inverted with a biasing phase wavelet, the inversion result is shown to be very consistent with true reflectivity. Even at a phase shift of 90 degree, an obvious phase rotation appears in the inversion results that is consistent with true reflectivity at most events. Rotation is caused by the rotated phase of the wavelet, but the result is fairly stable.

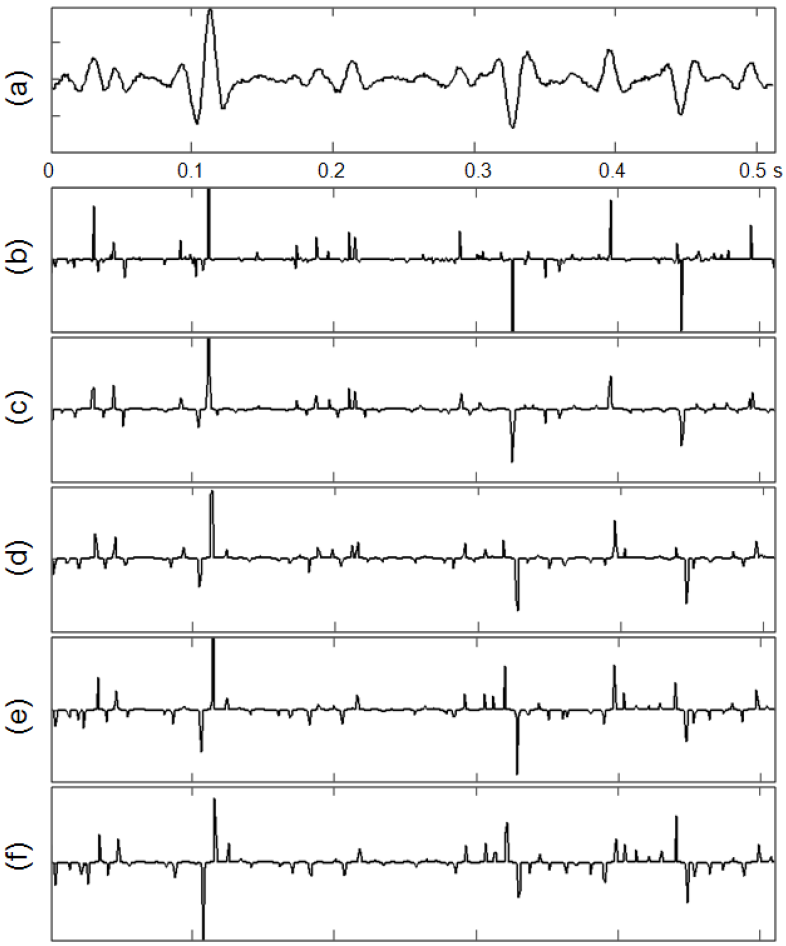

Figure 4.4: (a) shows the synthetic seismogram generated from a zero phase ricker wavelet with 10% random noise; (b) true reflectivity; (c) inverted reflectivity with a zero phase wavelet; (d) inversion reflectivity with a 30 degree phase wavelet; (e) inversion reflectivity with a 60 degree phase wavelet; (f) inversion reflectivity with a 90 degree phase wavelet

4.2 Sensitivity of Random Noise

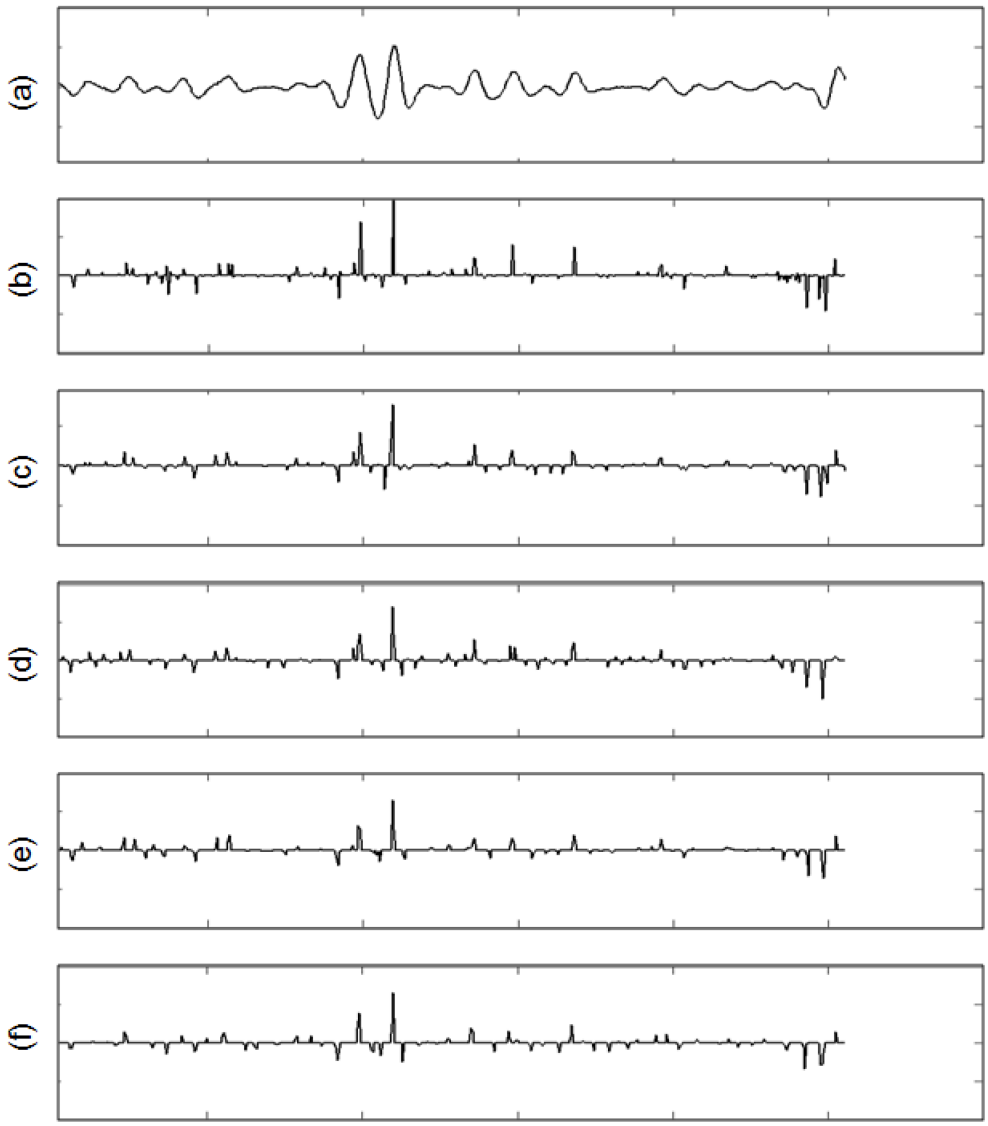

Figure 4.5: (a) True reflectivity; (b) inverted reflectivity with 5% random noise; (c) inverted reflectivity with 10% random noise; (d) inverted reflectivity with 20% random noise; (f) inverted reflectivity with 40% random noise;

Noise sensitivity is also critical to the BPI method. Noise cannot be avoided, only suppressed. In this section, we test the effect of random noise on BPI. Figure

4.5 (a) shows a synthetic seismogram that is generated from the convolution of a random reflectivity (shown in Figure 4.5 (b)) with a 40Hz ricker wavelet. The synthetic seismogram is first contaminated with 5%, 10%, 20% and 40% random noise, then BPI is implemented. Figure 4.5 (c), (d), (e) and (f) show the BPI result under 5%, 10%, 20% and 40% noise level.

To get the best inversion result, different balances between noise and resolution are pursued at different noise levels. In these tests, inverted reflection coefficients are shown to become lower with noise levels increasing because as more noise needs to be suppressed, more signal energy has to be sacrificed. To live up with noisy world, inverted reflectivity should be proportional to true reflectivity, which means consistent of the inversion results should be obtained. In this way, most events from the model reflectivity series are retained in the inversion results.

4.3 Comparison to Sparse Spike Inversion (SSI)

As known, SSI has been used widely in industry for many years. The two most commonly used products are Hampson-Russell and Fugro-Jason SSI. Hampson-Russell SSI uses a linear program described by **?**; the Fugro-Jason SSI algorithm is described by **?**, **?** and **?**. In contrast to BPI, both Hampson-Russell and Fugro-Jason SSI only solve the *primal* linear program shown in Eq. 2.9. The same parameter of sparseness is used to control the sparseness of the inverted results. In contrast, the trade-off factor λ in BPI plays a similar role to control the inversion result. In

practice, to get the best result, the proper parameter setting for any field data application is decided from a pretest. In this section, we compare apples to apples, by varying the trade-off factors to compare the best results obtained under SSI and BPI methods. After the 1-D synthetic test, we calculate the correlation between inverted and true reflectivity, which quantitatively evaluates the inversion results; The best results from SSI are compared to the best from BPI.

Figure 4.6 (a) and (b) show a synthetic seismogram and true reflectivity; 10% random noise is added. Figures 4.6 (c) and (d) show inversion results with small λ_{ssi} quantities that boost up the noise. Figures 4.6 (g) and (h) show large trade-off factor that create sparse inverted reflectivity. Too small and too large trade-off factors each lead to a discrepancy from true reflectivity. The best inversion results are located between 10^{-4} and 10^{-3}, so we test using with λ_{ssi} between 10^{-4} and 10^{-3}. Although we only show inversion results with λ_{ssi} ranging from 2×10^{-4} to 7×10^{-4}, many more tests were performed. The correlation between inverted and true reflectivity is plotted in Figure 4.7. This plot shows that the maximum correlation is around 0.8, with λ_{ssi} around 2×10^{-4}.

Figure 4.8 shows the BPI results. We present the small trade-off factor results in Figure 4.8 (c) and (d). As with the SSI results, noise is amplified. Figure 4.8 (g) and (h) show large λ_{bpi} that produce sparse inverted results. Too small and too large λ_{bpi} lead to the same effect on inversion results under both SSI and BPI. In this case, the best BPI result is located between 2 and 3. The results of intense scanning of λ_{bpi} are shown at Figure 4.8 (i)–(n). The correlation of BPI and true inverted is plotted at

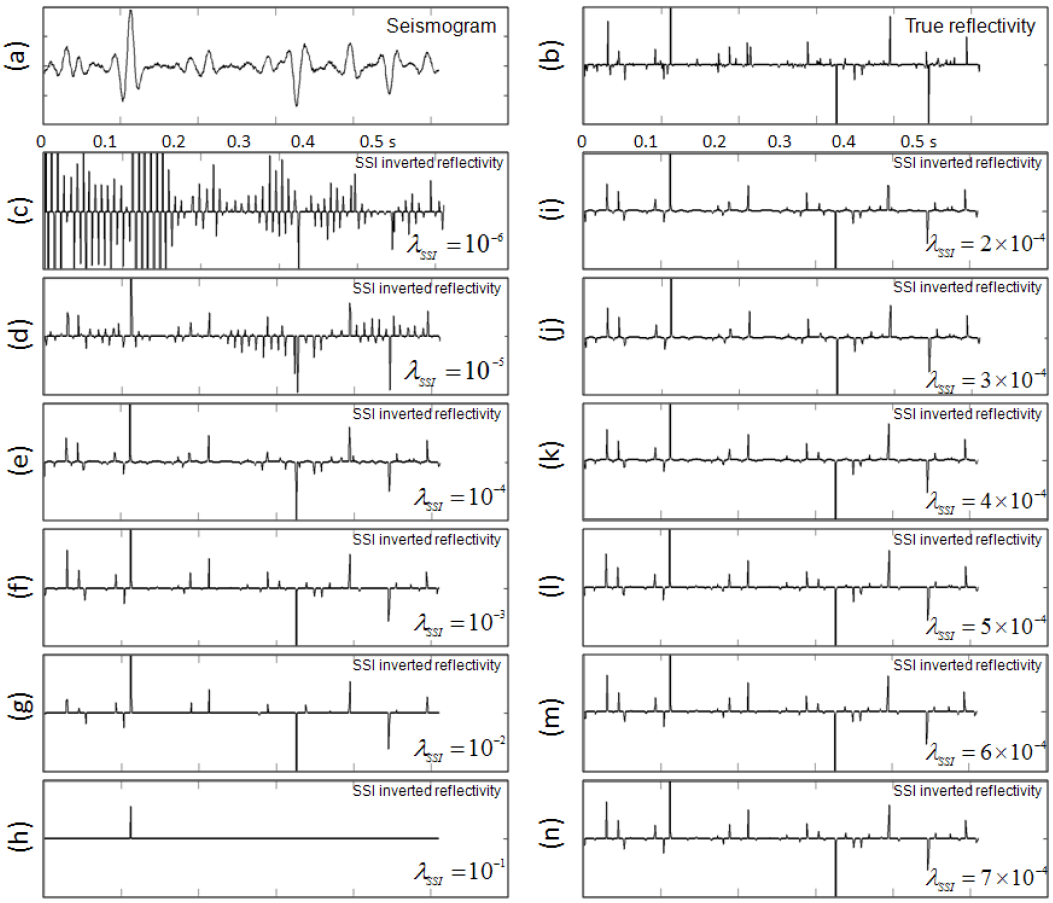

Figure 4.6: (a) Synthetic seismogram with 40 Hz ricker wavelet and random noise; (b) true reflectivity; (c) to (n) show SSI results with varying λ_{ssi} value; (c) $\lambda_{ssi} = 10^{-6}$; (d) $\lambda_{ssi} = 10^{-5}$; (e) $\lambda_{ssi} = 10^{-4}$; (f) $\lambda_{ssi} = 10^{-3}$; (g) $\lambda_{ssi} = 10^{-2}$; (h) $\lambda_{ssi} = 10^{-1}$; (i) $\lambda_{ssi} = 2 \times 10^{-4}$; (j) $\lambda_{ssi} = 3 \times 10^{-4}$; (k) $\lambda_{ssi} = 4 \times 10^{-4}$; (l) $\lambda_{ssi} = 5 \times 10^{-4}$; (m) $\lambda_{ssi} = 6 \times 10^{-4}$; (n) $\lambda_{ssi} = 7 \times 10^{-4}$.

Figure 4.9. The maximum correlation is approximately 0.9 located around 2.2. This synthetic test shows that the BPI method has apperant advantage over SSI method

Because L_1 norm minimization leads to the spiky series of the solution, λ balances sparseness with resolution in both BPI and SSI. But BPI can produce a better result than SSI if we choose the proper λ. Parameter λ acts as a trade-off parameter

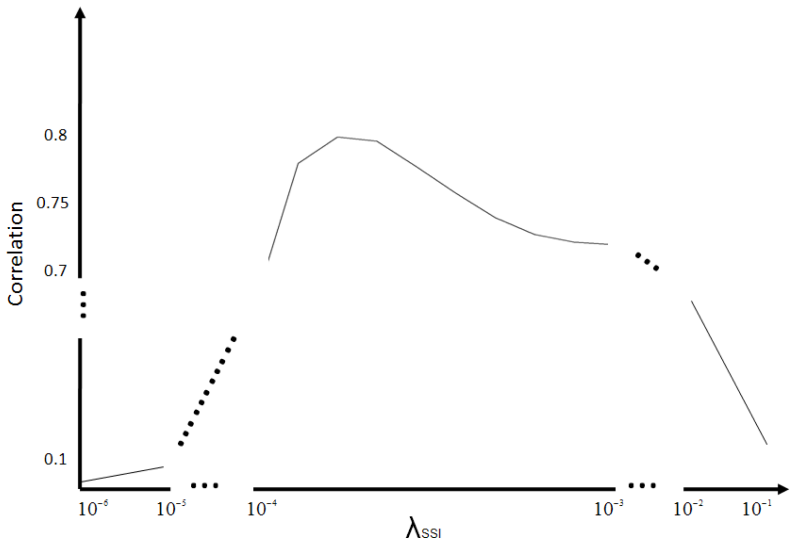

Figure 4.7: $\lambda - correlation$ curve of SSI. The correlation between SSI and true reflectivity is plotted according the trade-off factor λ_{ssi}

between underestimating the reflectivity and underestimating the noise. The reflectivity will always be underestimated when minimizing the L_1 norm of the reflectivity and noise when the signal to invert is contaminated with noise. The magnitude of the underestimation increases with the noise level. Parameter λ affects the resolving power of the inversion method. When more complex reflector configurations have to be resolved, a decreasing λ is required; when stronger noise realizations must be resolved, an increasing λ is required.

When minimizing the L_1 norm of the reflectivity and the noise, λ influences only the resolutions not the magnitudes of the underestimation of the reflectivity or noise. When the objective function to minimize is not entirely L_1, there is a trade-off between resolution and underestimation of the reflectivity. The a *priori* power, the desired error and the desired resolution of the reflectivity and noise and the objective function

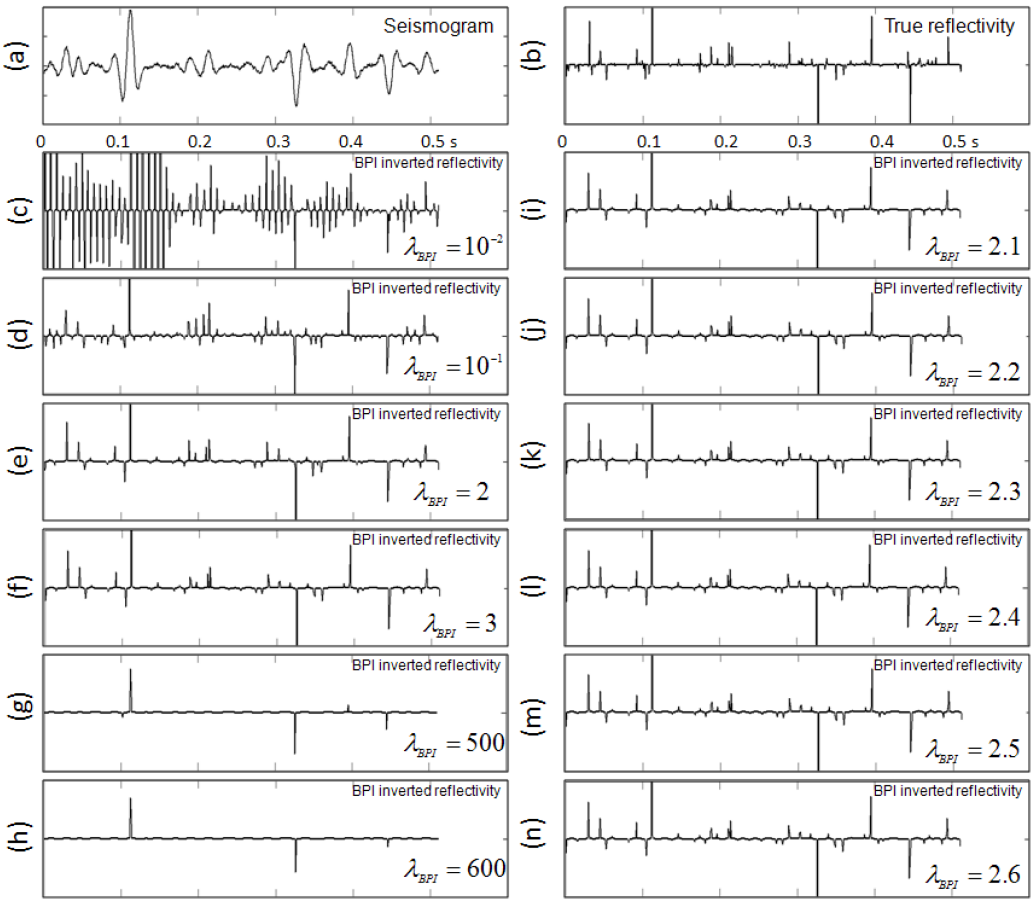

Figure 4.8: (a) Synthetic seismogram with 40 Hz ricker wavelet and random noise; (b) true reflectivity; (c) to (n) show BPI results with varying λ_{bpi} value; (c) $\lambda_{bpi} = 10^{-2}$; (d) $\lambda_{bpi} = 10^{-1}$; (e) $\lambda_{bpi} = 2$; (f) $\lambda_{bpi} = 3$; (g) $\lambda_{bpi} = 500$; (h) $\lambda_{bpi} = 600$; (i) $\lambda_{bpi} = 2.1$; (j) $\lambda_{bpi} = 2.2$; (k) $\lambda_{bpi} = 2.3$; (l) $\lambda_{bpi} = 2.4$; (m) $\lambda_{bpi} = 2.5$; (n) $\lambda_{bpi} = 2.6$.

to be minimized are all parameters in the choice of the optimum trade-off parameter λ. Therefore, there will always be a trade-off between noise and reflectivity, and between sparsity and accuracy. The conclusions may, therefore, only be used as rough qualitative guidelines and cannot be interpreted quantitatively. Parameter λ is too complex to be optimized analytically.

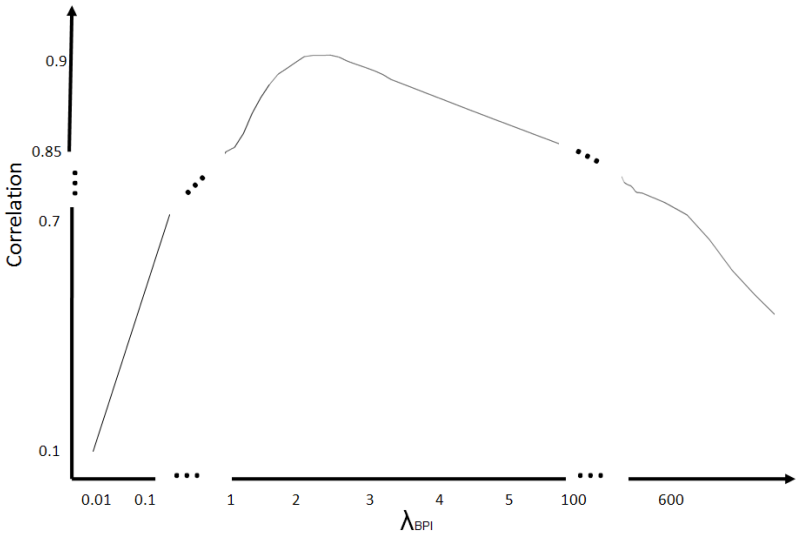

Figure 4.9: $\lambda - correlation$ curve of BPI. The correlation between BPI and true reflectivity is plotted according the trade-off factor λ_{bpi}

4.4 2D Synthetic

In this section, we produce wedge models with a 1-ms sample rate for a predominantly odd reflection- coefficient pair, $r_1 = 0.1$ and $r_2 = 0.2$ (in Figure 4.10 (a)), and a predominantly even reflection-coefficient pair, $r_1 = 0.1$ and $r_2 = -0.2$ (in Figure 4.10 (b)). The thickness increases from 1ms to 20ms. The tuning thickness of a thin-bed model with a Ricker wavelet is given by **?**. Eq. 4.1

$$t_R = \frac{\sqrt{6}}{2\pi f_0}, \tag{4.1}$$

where f_0 is the dominant wavelet frequency. For a 40Hz Ricker wavelet, $t_R = 10$ ms.

To achieve a more realistic model, we test the model with zero and 10% noise levels. The forward-modeling procedure is illustrated in Figure 4.10. We test both

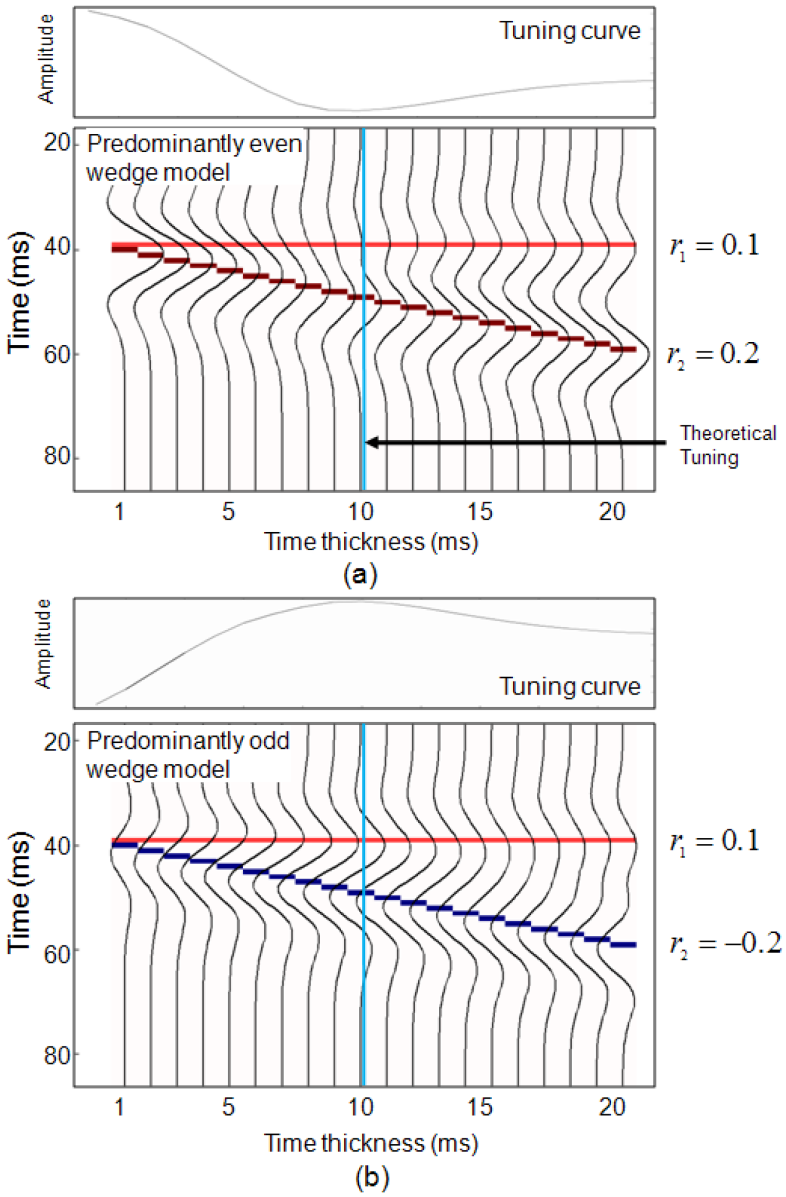

Figure 4.10: Original reflectivity wedge models for (a) an odd wedge and (b) an even wedge. Seismic data is generated with a 40-Hz Ricker wavelet convolved with the reflection-coefficient pair (black wiggles). Tuning thickness is 10ms.

BPI and SSI algorithms at noise free and with 10% noise levels. Figure 4.11 shows the noise free inversion results for the predominately even wedge model. Figure 4.11 (a)

and (b) show the best BPI and SSI inverted reflection coefficients with $\lambda_{BPI} = 10^{-2}$ and $\lambda_{SSI} = 10^{-7}$. Figure 4.11 (c) and (d) show the corresponding residuals which are subtractions of the true reflectivities from inverted reflectivities. The BPI residual values (in Figure 4.11 (c)) are small at thickness of 2 and 3 ms, while the SSI residuals (in Figure 4.11 (d)) show obvious values at thicknesses from 2 to about 5 ms.

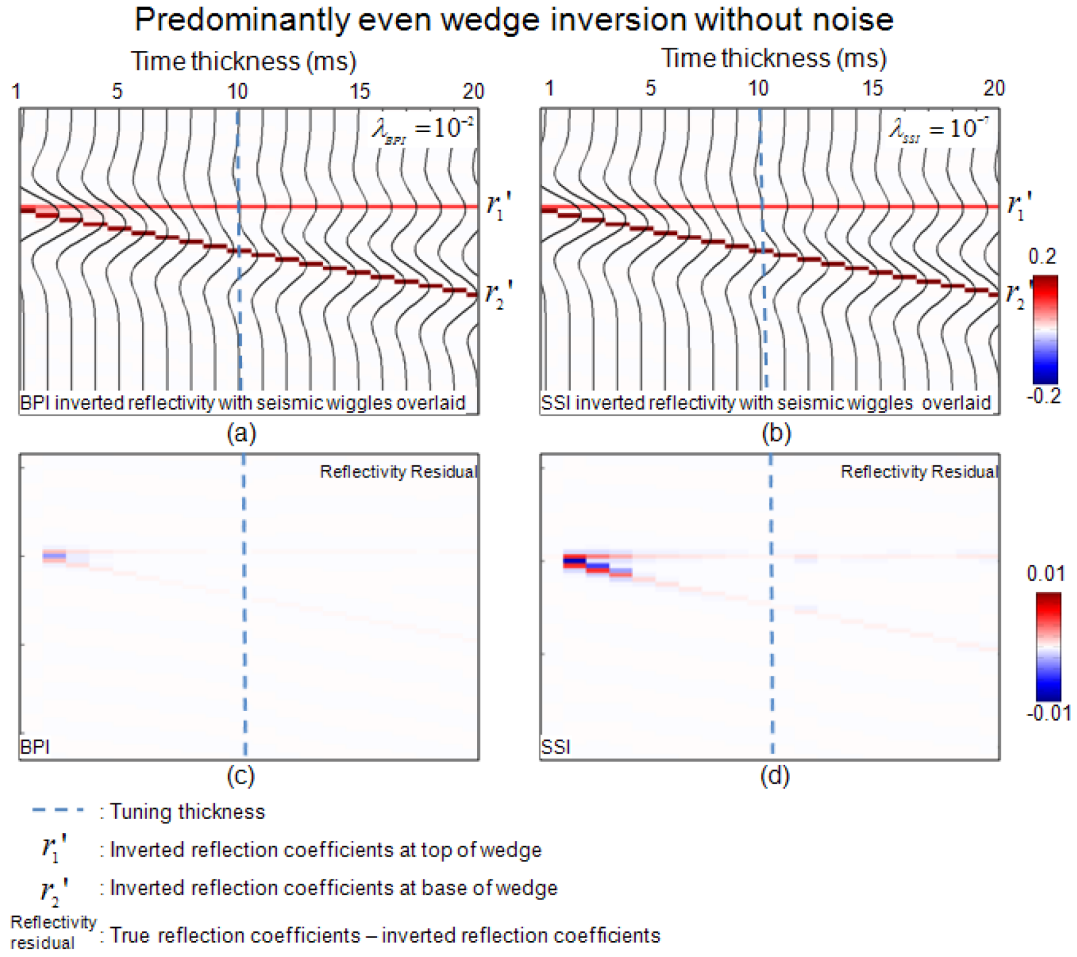

Figure 4.11: Inverted reflectivity for predominately even wedge model. (a) BPI inverted results with $\lambda_{BPI} = 10^{-2}$. (b) SSI inverted results with $\lambda_{SSI} = 10^{-7}$. (c) Residuals from BPI inverted results. (d) Residuals from SSI inverted results.

Figure 4.12 (a) and (b) show the best BPI and SSI results for the predominately

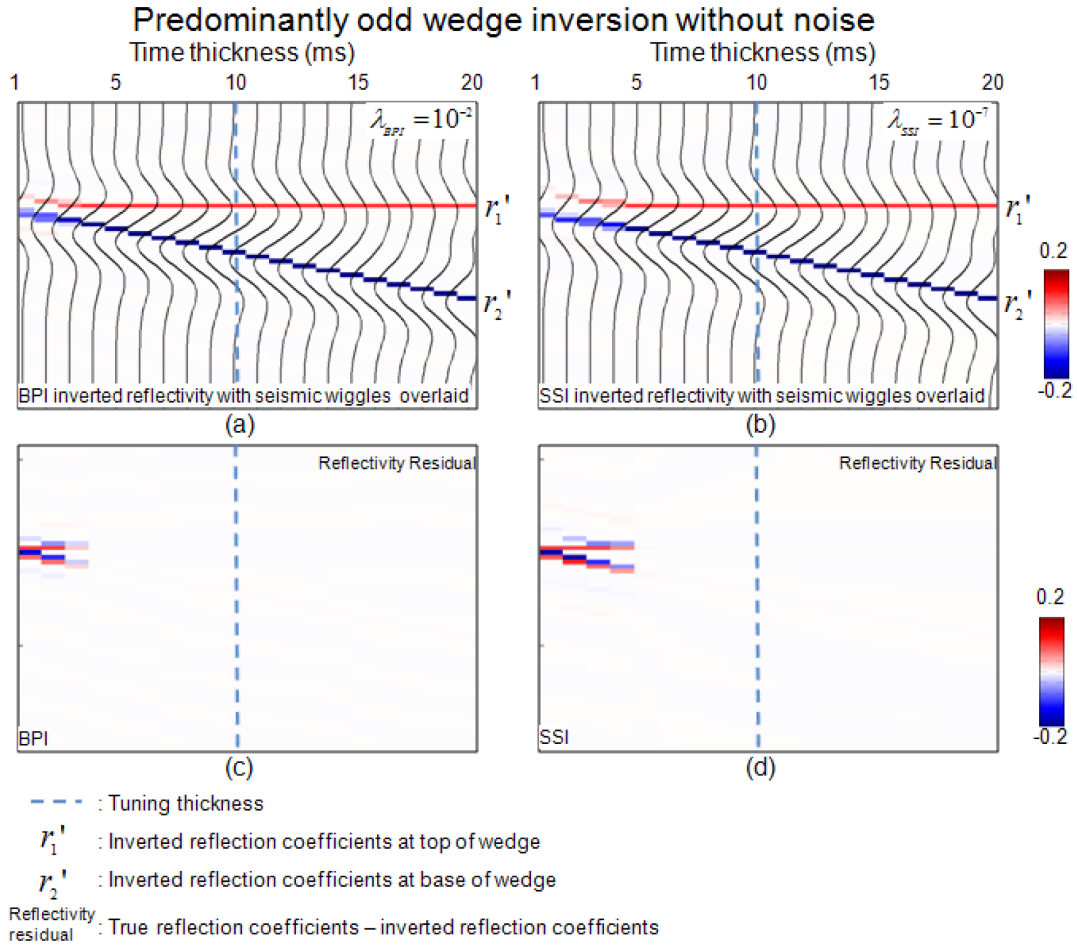

Figure 4.12: Inverted reflectivity for predominately odd wedge model. (a) BPI inverted results with $\lambda_{BPI} = 10^{-2}$. (b) SSI inverted results with $\lambda_{SSI} = 10^{-7}$. (c) Residuals from BPI inverted results. (d) Residuals from SSI inverted results.

odd wedge model. Figure 4.12 (c) and (d) show the residuals of BPI and SSI, respectively. The BPI results (in Figure 4.12 (c)) show obvious residuals at thicknesses from 1 to 3 ms, while SSI results (in Figure 4.12 (d)) show residuals from 1 to 4ms.

Figure 4.13 shows the BPI and SSI inversion results of the predominantly even wedge model with an S/N ratio of 10. Figure 4.13 (a) and (b) show the BPI and SSI inverted results with $\lambda_{BPI} = 2$ and $\lambda_{SSI} = 10^{-3}$, respectively. Figure 4.13 (c)

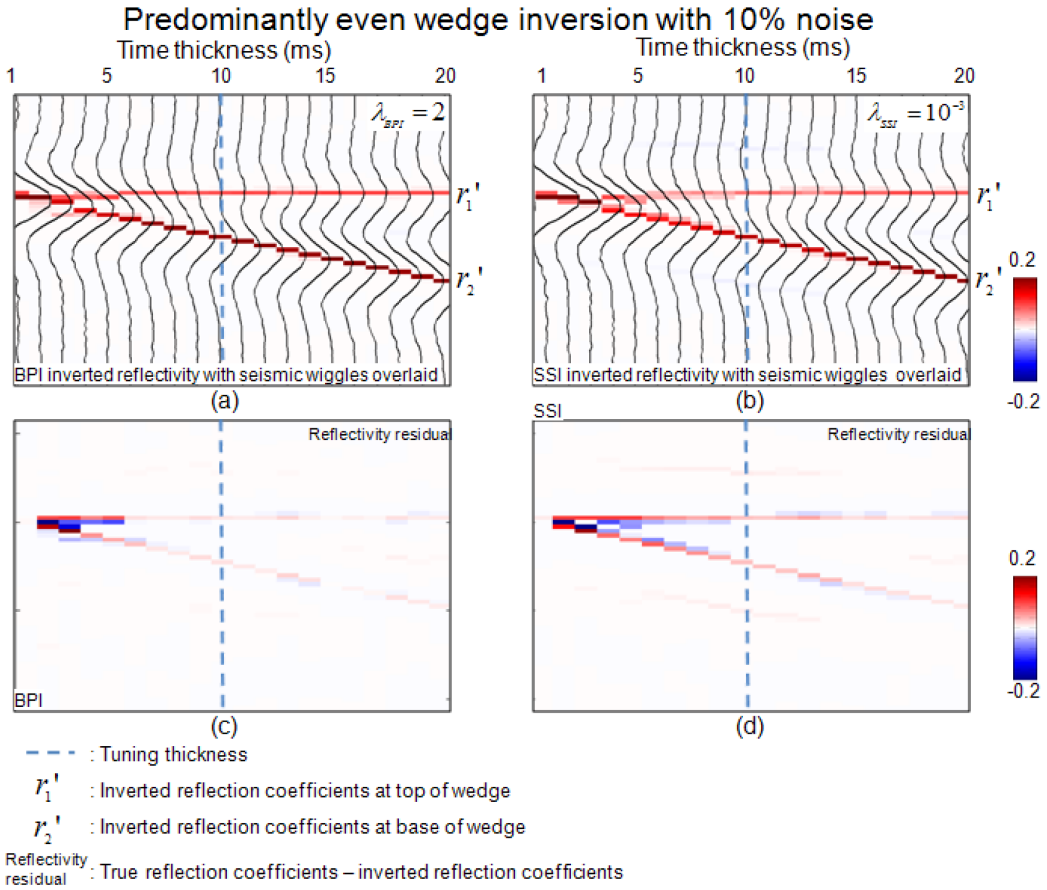

Figure 4.13: Inverted reflectivity for predominately even wedge model with 10% noise. (a) BPI inverted results with $\lambda_{BPI} = 2$. (b) SSI inverted results with $\lambda_{SSI} = 10^{-3}$. (c) Residual from BPI inverted results. (d) Residual from SSI inverted results.

and (d) show the corresponding residuals. Figure 4.13 (c) shows residuals of BPI at thicknesses from 2 to 6 ms while Figure 4.13 (d) shows apparent residuals at thicknesses from 2 to 15 ms.

Figure 4.14 (a) and (b) show the BPI and SSI inversion results of the predominantly odd wedge model with an S/N ratio of 10. Figure 4.14 (c) and (d) show the corresponding residuals. The BPI results (in Figure 4.14 (c)) show obvious residuals

at thicknesses from 1 to 7ms and weak residual beyond 7 ms. Figure 4.14 (d) shows obvious residuals of SSI at thicknesses from 1 to 8 ms that decay beyond 8 ms.

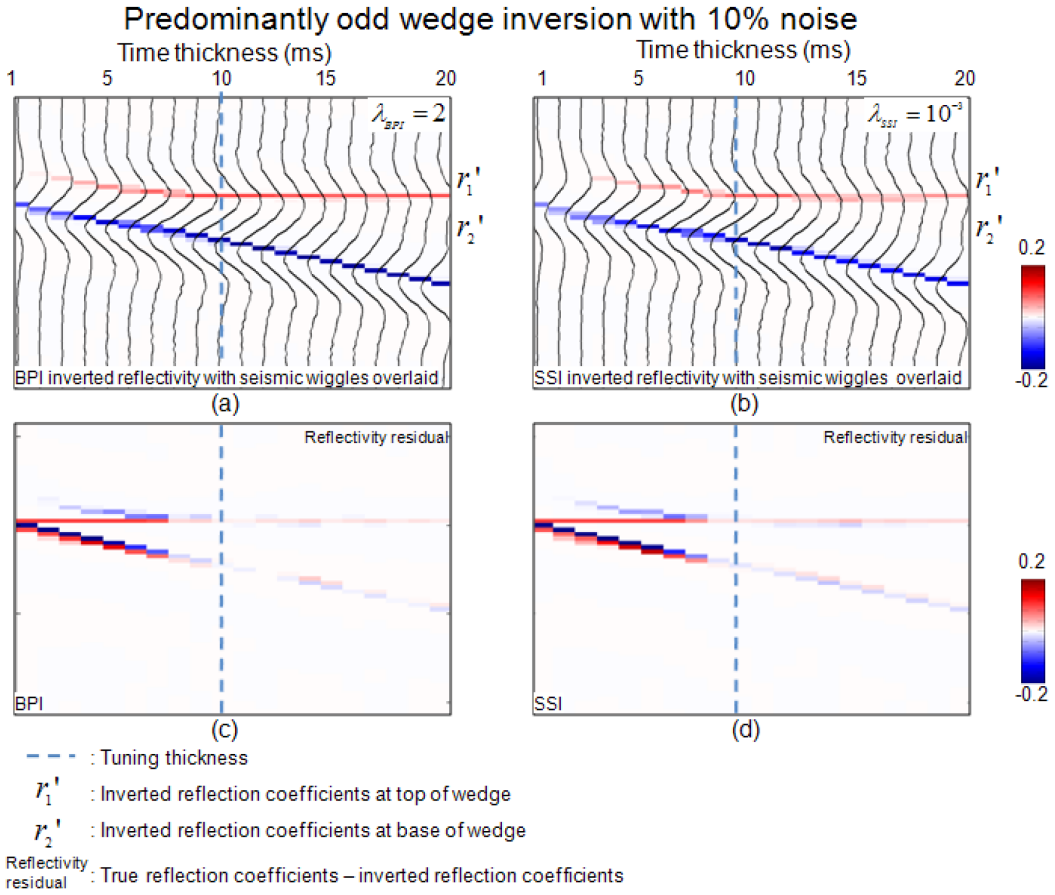

Figure 4.14: Inverted reflectivity for predominately odd wedge model with 10% noise. (a) BPI inverted results with $\lambda_{BPI} = 2$. (b)SSI inverted results with $\lambda_{SSI} = 10^{-3}$. (c) Residual from BPI inverted results. (d) Residual from SSI inverted results.

Because inversion is a trace by trace procedure, one may question its lateral continuity. We create a 2-D synthetic using a piece of the well-log reflectivity series to generate a 2-D complex wedge model. The middle part of the well-log reflectivity is thinned from left to right (as shown in Figure 4.15 (a)). Corresponding synthetic

seismic data is generated with a 30 Hz ricker wavelet. Figure 4.15 (c) shows the BPI inverted result with λ of 2.2. Figure 4.15 (d) shows the residual of true over inverted reflectivity. In this synthetic test, BPI shows good lateral continuity with superior vertical resolution. The BPI on this 2-D synthetic test is carried on trace-by-trace which also produces convincing results with superior vertical resolution and great lateral continuity. All of these synthetic tests lead to the confidence to the field data.

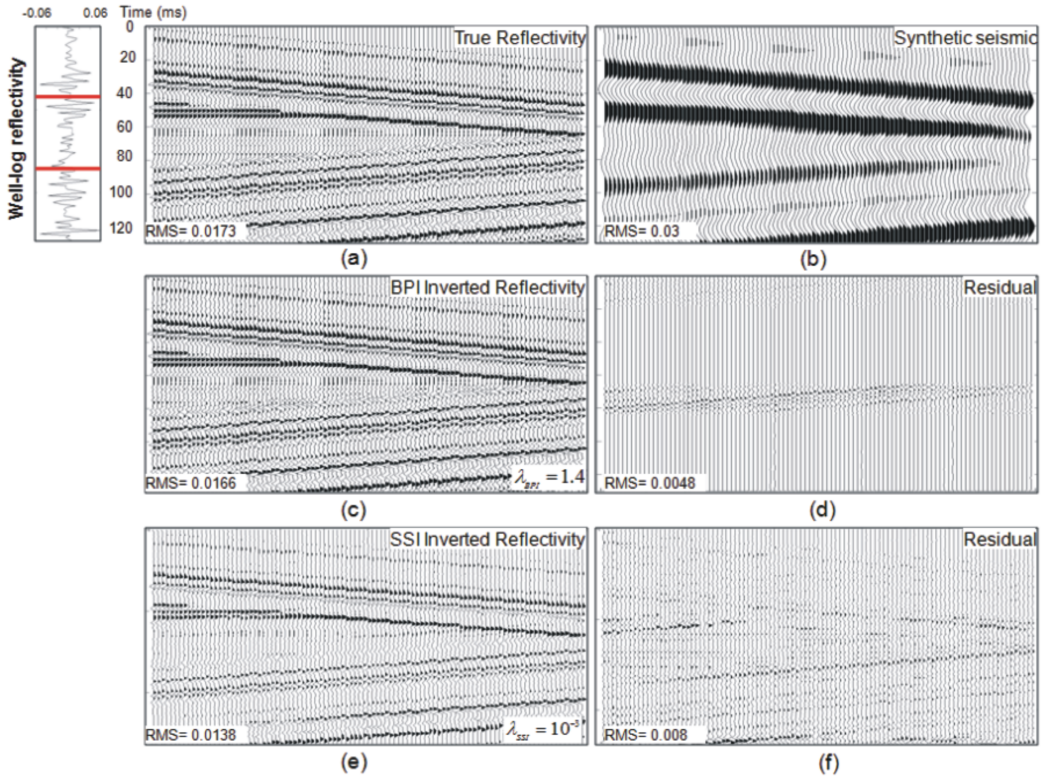

Figure 4.15: (a) True reflectivity; (b) synthetic seismogram with 10% random noise; (c)BPI inverted reflectivity with λ_{bpi} of 2.2; (d) residual of true over BPI inverted reflectivity; (e) SSI inverted reflectivity with λ_{ssi} of 10^{-3}; (f) residual of true reflectivity over SSI inverted reflectivity

Chapter 5

Application to Field Data

The fundamental difficulty when applying basis pursuit inversion (BPI) to real data is the fact that real data do not satisfy the convolution equation. In other words, a perfect tie between the synthetic and the seismic data at the well location is impossible (**?**).

If we insist a very good synthetic tie to be a prerequisite to the inversion, we will most like be frustrated. The convolution equation represents a much simplified earth model: zero-offset, normal incidence seismic on a one-dimensional medium. The poststack seismic image data on which we perform the inversion are usually the result of stacking prestack migration, which uses a velocity model to focus energy from different offset. The velocity model is rarely perfect, leading to incorrect event locations. The migration amplitude represents some kind of average of reflectivities from a large angle range. But most interpretation work is still carried on this poststack seismic image because it shows the geological structure. The calibrated wavelet used

here from the seismic well tie can be considered as the derivative of poststack seismic image data over well log reflectivity. It plays as jacobin kernel, as in all the other inverse problems. Our inversion method invert the poststack seismic image based on the well-log reflectivity model.

In the previous chapters, different synthetic tests show that BPI is doing well on 1-D and 2-D cases. In this chapter, we present various applications of BPI on real field data. Application I mainly focuses on the good fit between BPI results and well log impedance data, which highlights the convincingly superior vertical resolution. Application II focuses on the consistency of BPI reflectivity to the original seismic image data. Application III mainly shows the improvement of BPI results on stratigraphic interpretation by a comparison to SSI results. Applications IV and V show the example of how our BP inversion works on 3-D datasets and its impact on interpretation. Finally, application VI places a glance of application of BPI on prestack data that probably leads to lots of future work.

5.1 Application I

The first application is to test the correlation of BPI with the original seismic image and well-log data. Seismic image data (in Figure 5.1) is a piece of onshore datasets with a well located at the black rectangle. The well-log information for lithologic interpretation, including gamma ray, resistivity, is available at Figure 5.2.

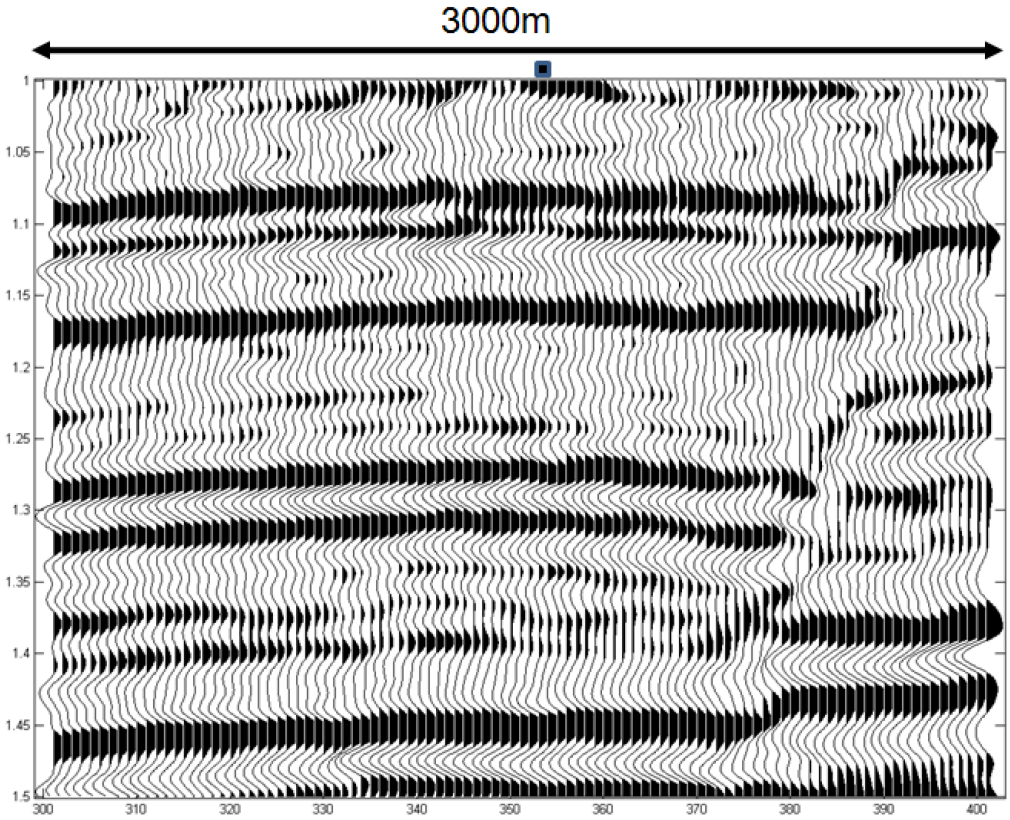

Figure 5.1: Original seismic image data with RMS amplitude of 6.1×10^4. A well is located at the place of black rectangle.

We created a synthetic tie between the input seismic data and the well-log data, stretching the well-log data to time without reference to the inverted data for an unbiased, quantitative layer-thickness comparison between the well-log data and the inverted data. In the original seismic tie to the well, at Figure (5.2), we achieved a relatively good fit $r = 0.79$ between the well-log reflectivity convolved with the extracted wavelet and the extracted seismic image trace.

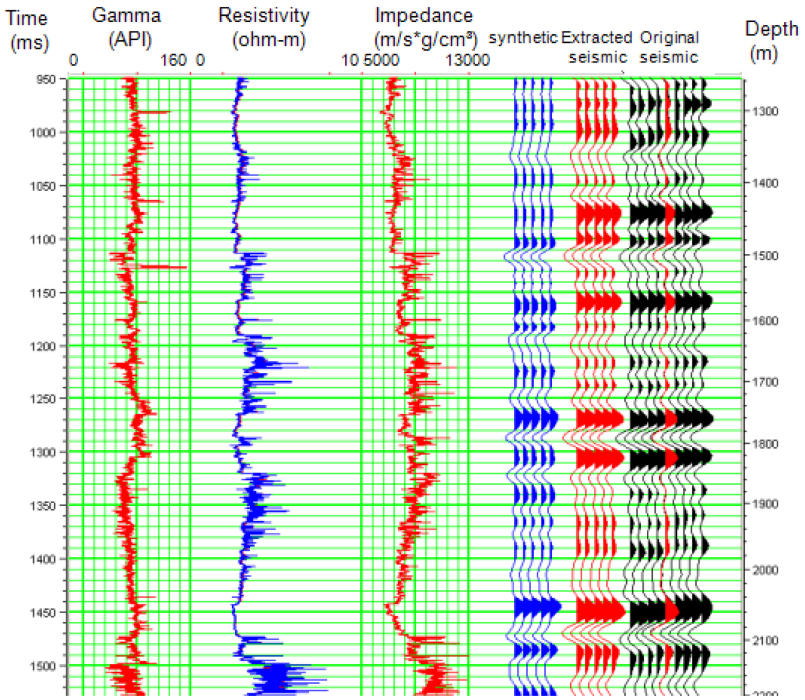

Figure 5.2: Well-log data, including resistivity, and computed impedance, along with the synthetic tie (blue), the trace at the well (red), and the seismic traces surrounding the well (black). The correlation coefficient r is 0.79

The wavelet extracted from the well for the synthetic is shown in Figure 5.3. The peak frequency of the wavelet is about 25 Hz, yielding a one-quarter-wavelength resolution of about 20 ms. The phase of the wavelet is about 140 degrees, leading to a negative polarity of seismic data.

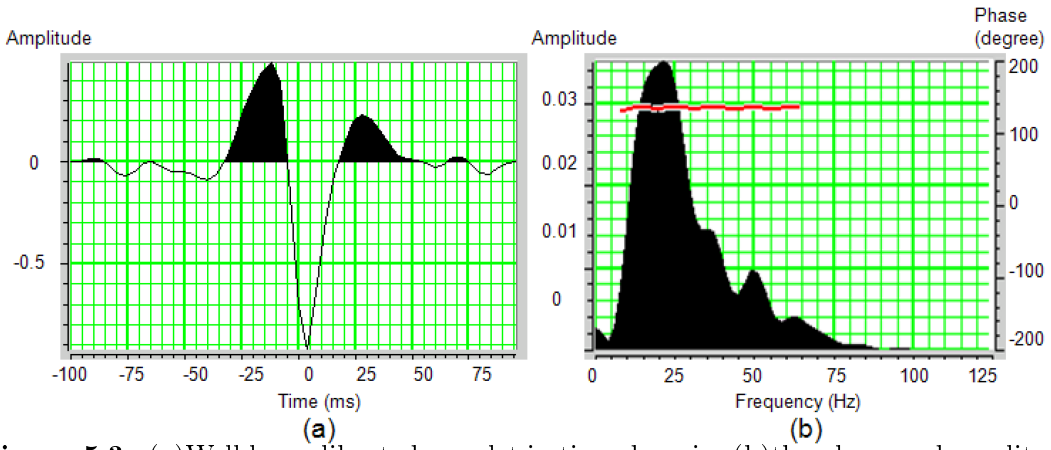

Figure 5.3: (a)Well log calibrated wavelet in time domain; (b)the phase and amplitude spectra of the wavelet. The peak frequency is about 25 Hz; phase is about 180 degree.

BPI is applied to the seismic image data (Figure 5.1) based on the calibrated wavelet (Figure 5.3). The BPI inverted reflectivity cross section is shown in Figure 5.4. However, doubts about the validity of the inversion result remain. Based on inversion theory, the validity of inversion results rely on the random distribution of the residual.

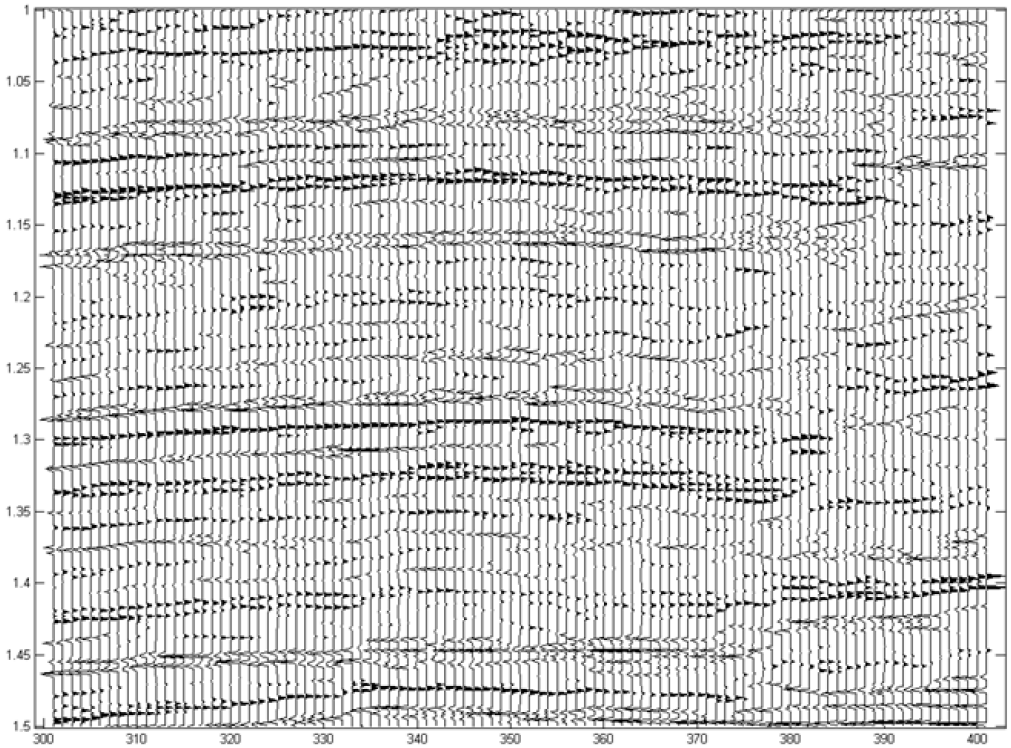

Figure 5.4: Inverted reflectivity section.

Figure 5.5 shows the residuals which is the subtraction of the original data by inverted reflectivity convolved with the wavelet. Comparing to the original seismic section with RMS amplitude as 6.1×10^4, the residual holds RMS amplitude of 2.2×10^3. The small magnitude of the residual demonstrates that the BPI remains constant with the seismic data. Such a random distributed 2-D error from BPI shows its robustness.

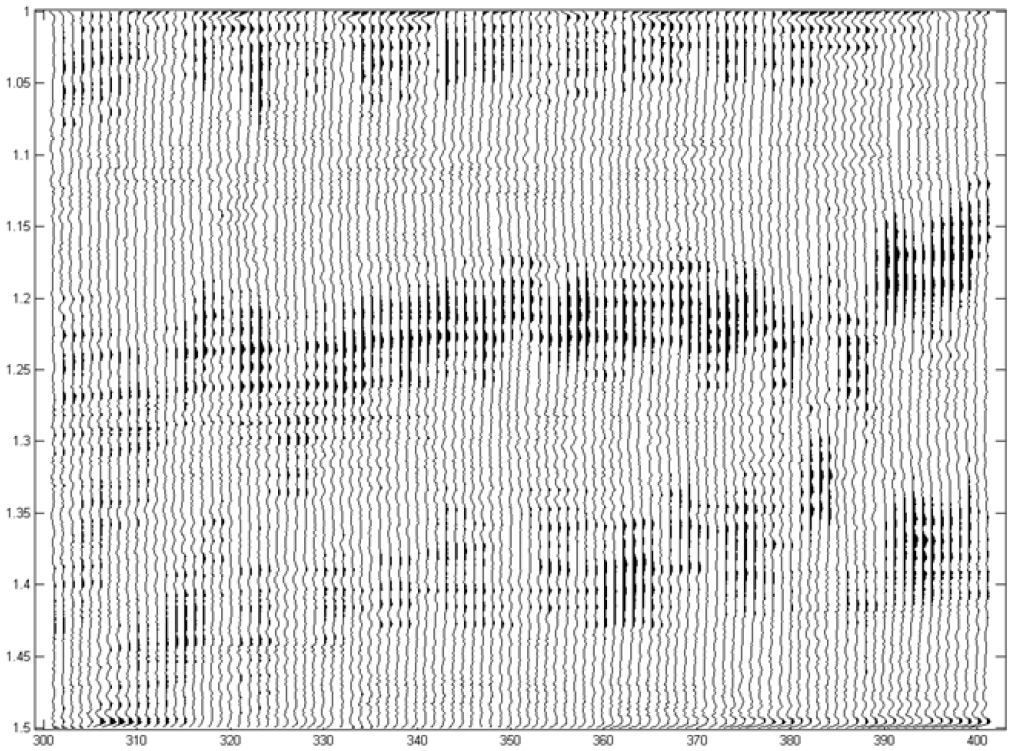

Figure 5.5: Residual between original data and inverted reflectivity convolving with the extracted wavelet with RMS amplitude $= 2.2 \times 10^3$.

We also visually compare the well-log data with the basis pursuit inverted relative impedance, (in Figures 5.6) where the well-log relative impedance is used to test the validity of our basis pursuit inversion processing. The relative impedance is the exponential integration of reflectivity. However, because the seismic data are much lower in frequency than the well-log data, the fit is useful only as an approximation for aligning gross lithologic packages. A great deal of useful information is lost due to the seismic wavelet. The BPI provides a significantly better representation of the layering observed in the log data than the original seismic data does. Figure 5.6 displays basis pursuit inversion impedance and well-log impedance in color. This figure emphasizes inverted relative impedance changes to provide a very good tie to the well with higher

fidelity. Through this good tie, the well log interpreted sand and shale packages (see Figure 5.2) can be easily extended into a seismic cross-section.

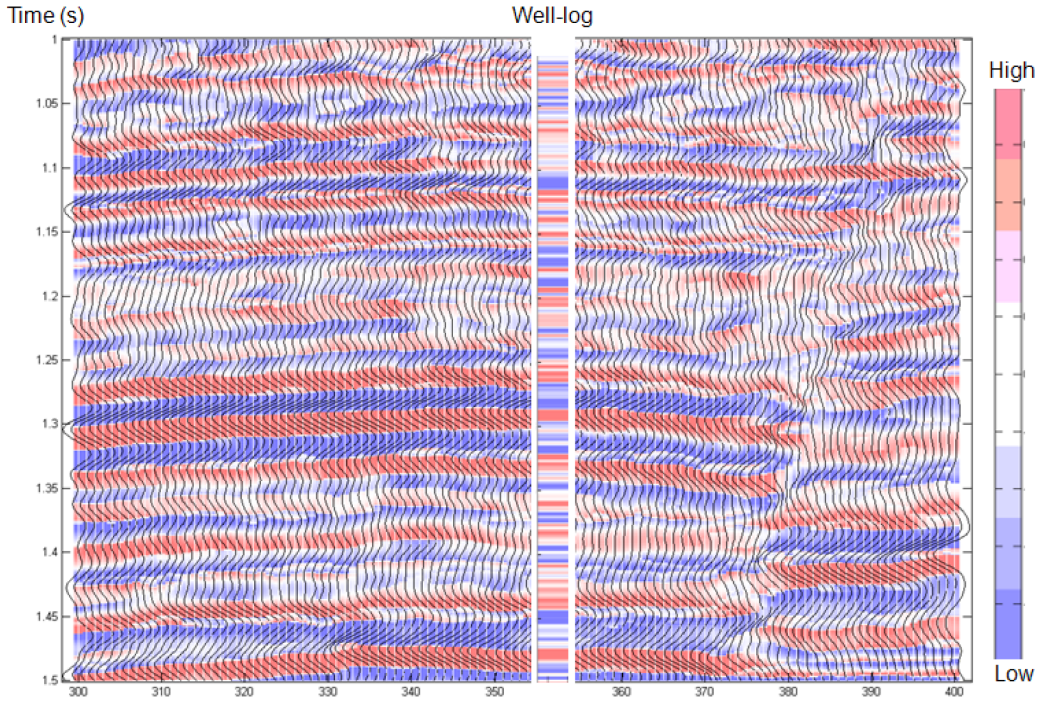

Figure 5.6: Comparison between basis pursuit inverted data and well log data with seismic image wiggles overlayed. The middle column is the well impedance low-cut filtered.

Viewing the comparison of BPI impedance to the overlayed original seismic image wiggles in Figure 5.6, it is clear that some boundaries between layers are indistinct on the original seismic section. Layers below the tuning thickness (20ms) are not resolved in the original seismic data. Geologic detail is obscured by the wavelet interference patterns, which become more apparent when compared with the inversion. A skilled interpreter can decipher meaningful information embedded in the wavelet-interference patterns, but it is desirable to remove these artifacts altogether to allow direct access to the underlying geology.

Generally, sands correspond to a lower gamma ray, higher resistivity and higher impedance; shales correspond to high gamma ray, lower resistivity and lower impedance. In the interval shown in Figure 5.7, a shale embed sands is indicated by gamma ray and the sands have higher impedance than the shales. The interpretation of well-log data shows a close correspondence to the inverted data. We observe that the sand-shale-sand sequence is resolved below the tuning thickness. The original seismic data (Figure 5.7 (c)) is compared with the well log and the BPI data (Figure 5.7 (b)). The original seismic data fails to delineate thin shale layering as compared with the inverted data. The inverted data resolves similar gradational changes within an individual layer as the impedance log (Figure 5.7 (a)).

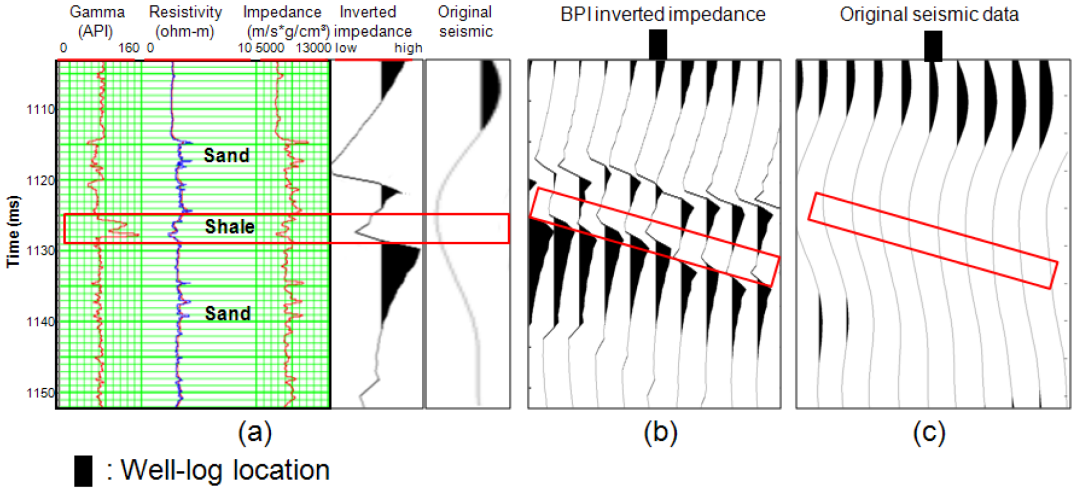

Figure 5.7: Well log (left) compared with BPI data (middle) and original seismic image data (right). Well log location is indicated by the black rectangle on the top. Shale are indicated by of higher gamma ray and low impedance in this interval.

A Comparison of the well-log impedance to the inverted impedance, shows the thickness inversion layering below the tuning thickness (the peak frequency of the data is 25 Hz, yielding a one-quarter-wavelength resolution of about 20 ms). Figure 5.7

shows a well-resolved sand-shale-sand sequence that has a embedded shale thickness of 3 ms (about 10 meters), which is much thinner than the tuning thickness (Figure 5.7). Although the thickness inversion effectively delineates the layering sequence below tuning, it also captures gradational impedance changes within thin layers, as in the case of sand grading into shale. Through BPI relative impedance, it is much easier to pick out the shale layer that has already been indicated by well log data.

5.2 Application II

This example demonstrates the vast improvement in vertical resolution for discrete layers that is achieved by using basis pursuit inversion rather than other inversion methods. Figure 5.8 shows an OBC dataset from the Gulf of Mexico, where the black filled rectangle shows the well-log location. The well-log calibrated wavelet spectrum is shown in Figure 5.9. By using BPI, inverted reflectivity is shown in Figure 5.10.

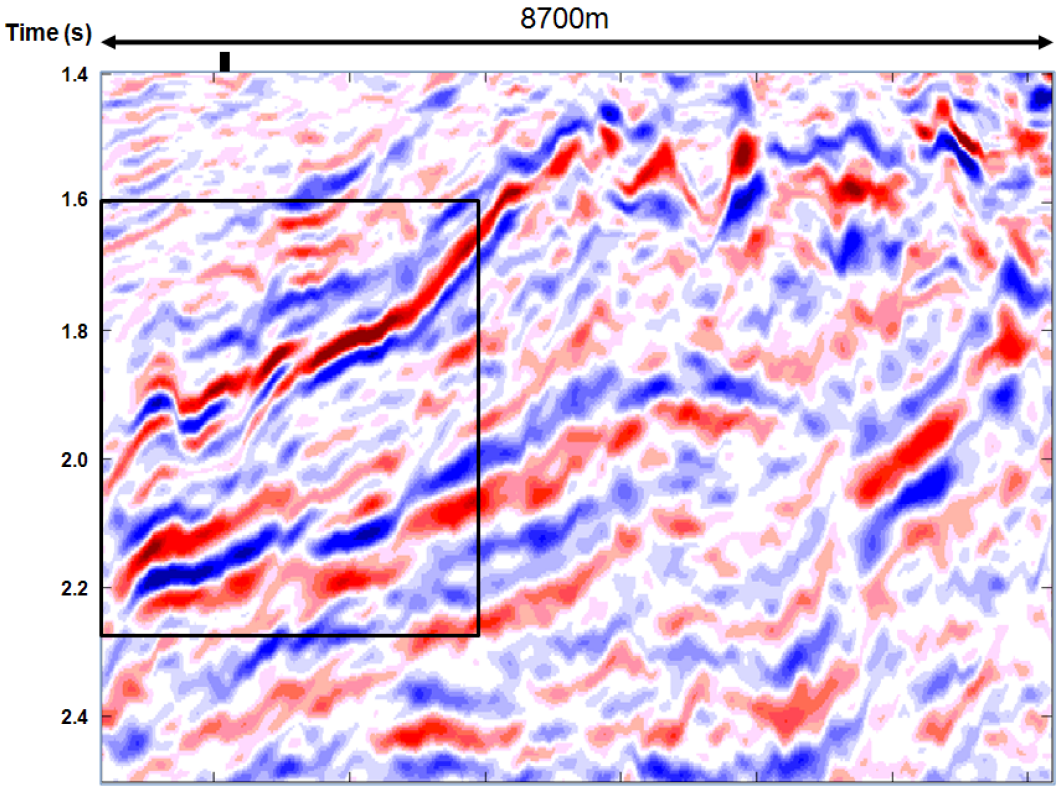

Figure 5.8: Seismic data from the Gulf of Mexico. The detailed result within the black rectangle will be analyzed later.

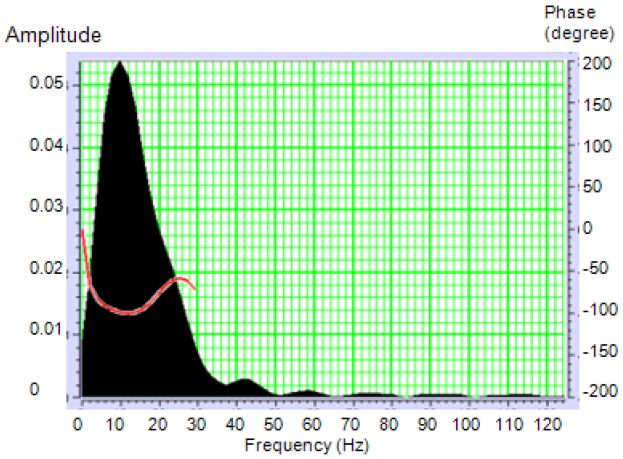

Figure 5.9: The phase and amplitude spectra of the wavelet extracted from the seismic well tie. The peak frequency is 10 Hz.

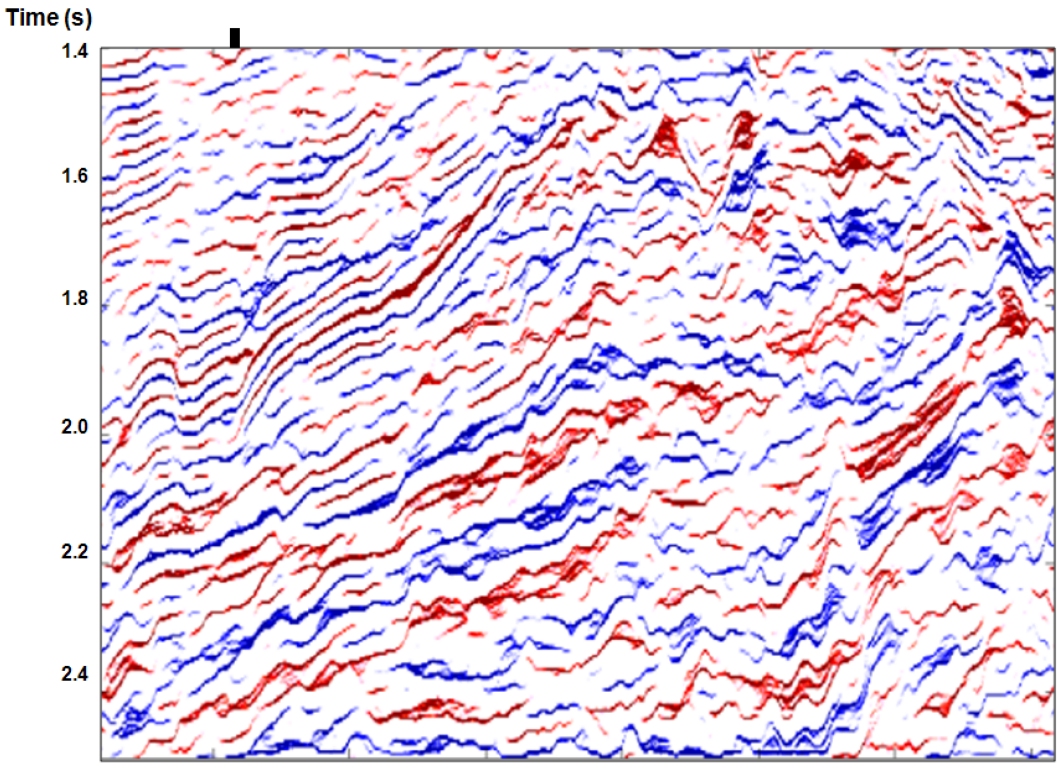

Figure 5.10: BPI inverted reflectivity from field data, shown in Figure 5.8. Red is positive; blue is negative.

Inverted reflectivity has the wavelet effect absolutely removed. Such a reflectivity cross-section gives a much clearer view of the subsurface than seismic data, which is a "blur" image caused by the wavelet effect. The reflectivity cross-section not only gives the magnitude of the impedance contrast but also the accurate location the the interface. Both the position and the amplitude of the reflectivity are very helpful in locating and evaluating the reservoir. Using this reflectivity section, an interpreter can easily pick the horizon by following the reflectivities. Here, the positive reflection coefficients mean a low to high impedance transaction. Vice verse.

Figure 5.11 shows the smaller piece from the black rectangle in Figure 5.8; Figure

5.12 shows BPI inverted reflectivity.

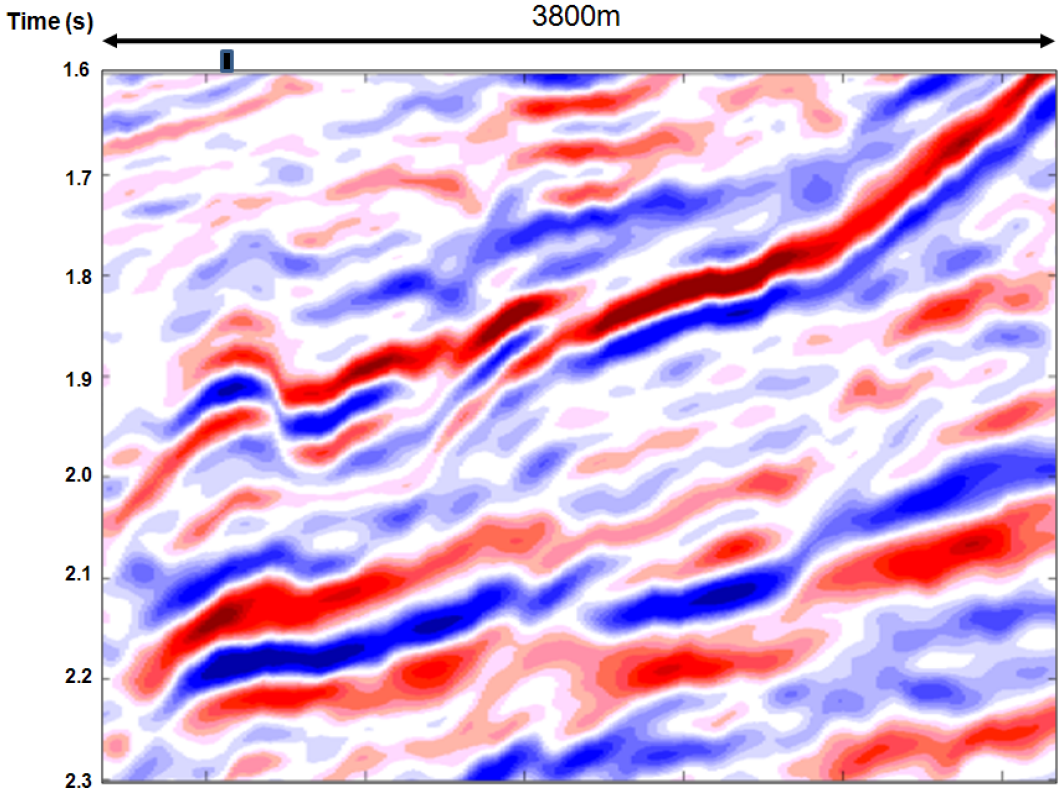

Figure 5.11: The small piece of data within the black rectangle in Figure 5.8

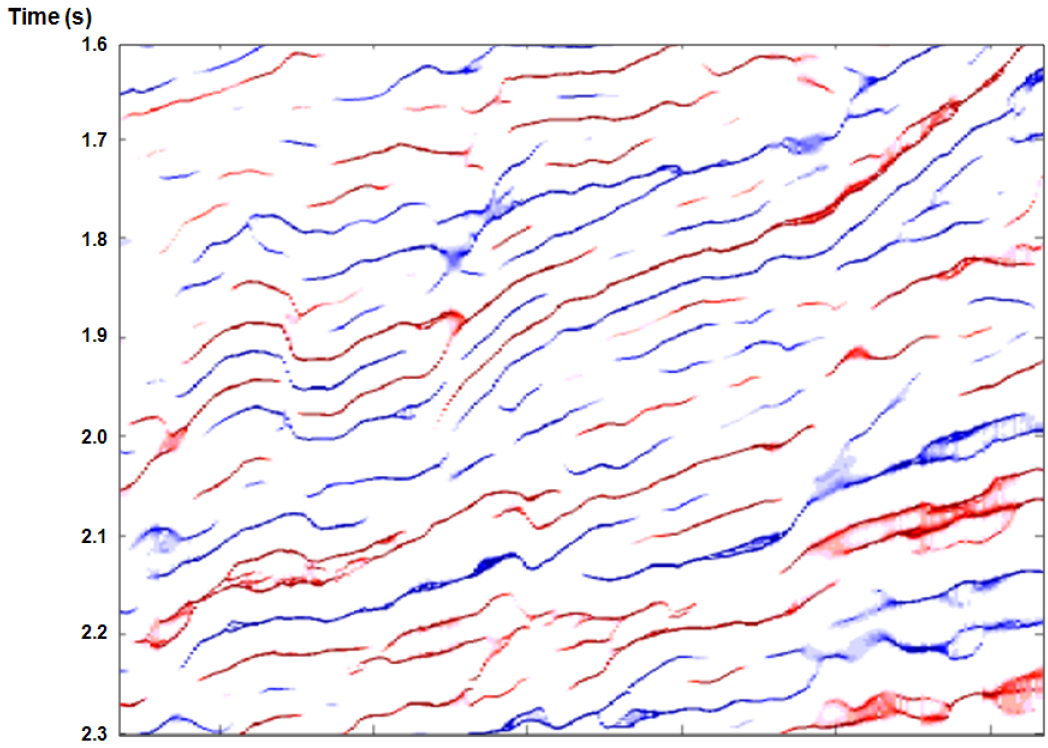

Figure 5.12: BPI Inverted reflectivity from Figure 5.11

A possible question that could crop up in an interpreter's mind is whether the extra level of reflection detail is genuine. An overlapping display of seismic data with reflectivity are shown in Figure 5.13. Figure 5.13 (a) shows a large scale of the image and (b) shows a detailed image. Because the wavelet used is approximately zero phase, reflectivities are mostly located at the peak and trough of the seismic. Such consistency of reflectivity and original seismic data makes it believable that all the results come from the seismic image data and not something else. Many thin-bed reflectivities have been resolved within a single positive of negative amplitude. As pointed by the blue arrow, multiple positive reflectors are resolved within the positive amplitude. The red arrow shows that multiple negative reflectors are resolved within

the negative amplitude.

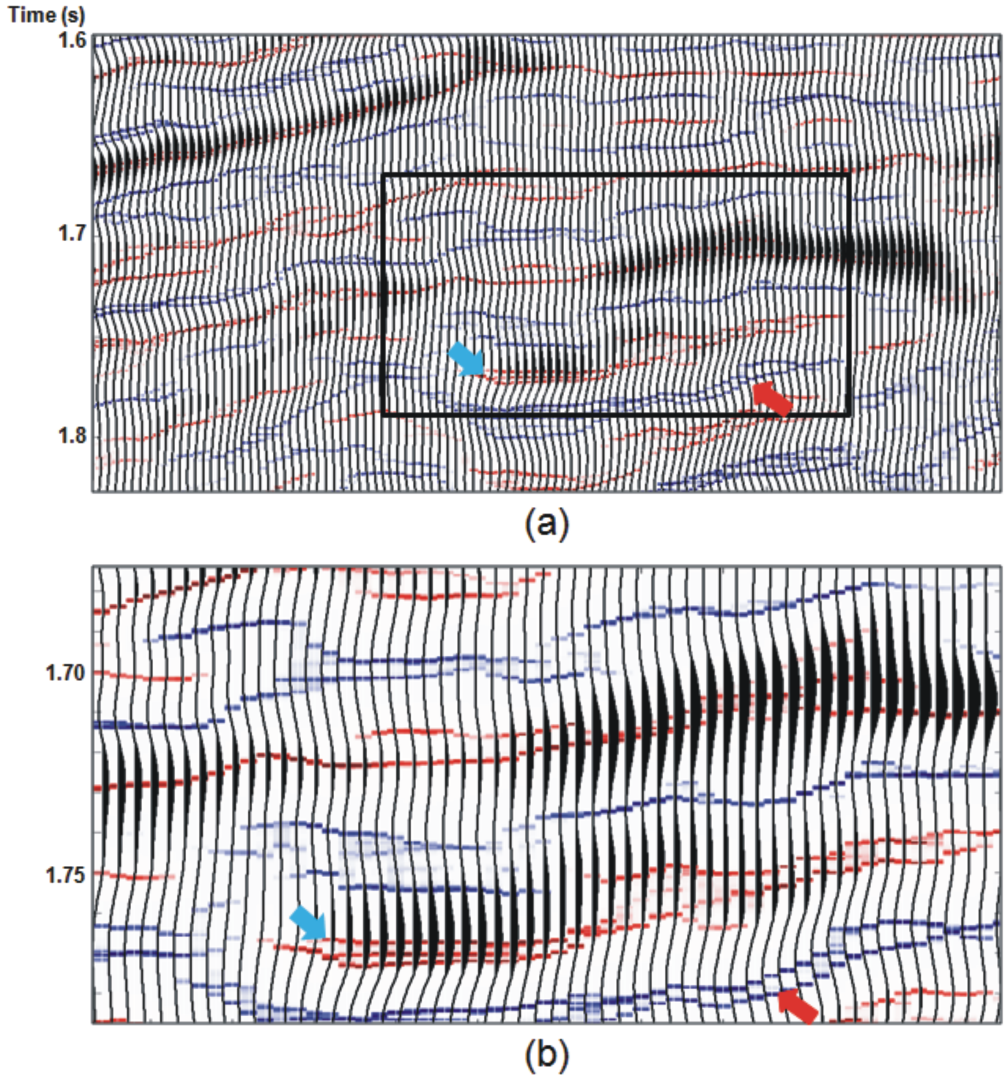

Figure 5.13: (a) Overlap display of original seismic data with reflectivity; (b) overlap display of original seismic data with reflectivity within the black rectangle in (a).

5.3 Application III

Basis pursuit inversion (BPI) takes advantage of L_1 norm minimization constraint, leading to a spiky result, and the wedge dictionary, leading to thin bed resolution. Thus it can resolve much more detail than conventional inversion methods, such as sparse spike inversion (SSI). In this section, we apply both SSI and BPI on the dataset contained in the previous section. Figures 5.14 – 5.18 show a comparison between BPI and SSI with relative impedance; the original seismic image wiggles are overlayed. The calibrated wavelet used here holds peak frequency of about 8Hz with a phase of zero. The tuning thickness of this data is about 50 ms.

Figure 5.14 (b) shows an SSI result. It captures those major contrasts in consistency with seismic image wiggles. For example, positive wiggles correspond to a low to high impedance change within the yellow rectangle. Figure 5.14 (a) displays BPI results that resolve many more thin layers than the conventional sparse spike method. An original seismic image is also taken into comparison showing that basis pursuit can resolve several layers within one seismic cycle, while conventional sparse spike can only resolve three layers.

Figure 5.15 shows another example of how basis pursuit inversion helps interpretation. Seismic image wiggles show a single horizon possibly picked along the peak amplitude at this cross-section at about 2.1s. Basis pursuit inversion (in Figure 5.15 (a)) not only gives much higher resolution than sparse spike inversion (in Figure 5.15 (b)), but probably leads to a totally different interpretation. A couple of possible updip layers are indicated by white arrows (in Figure 5.15 (a) and (b)) which are not

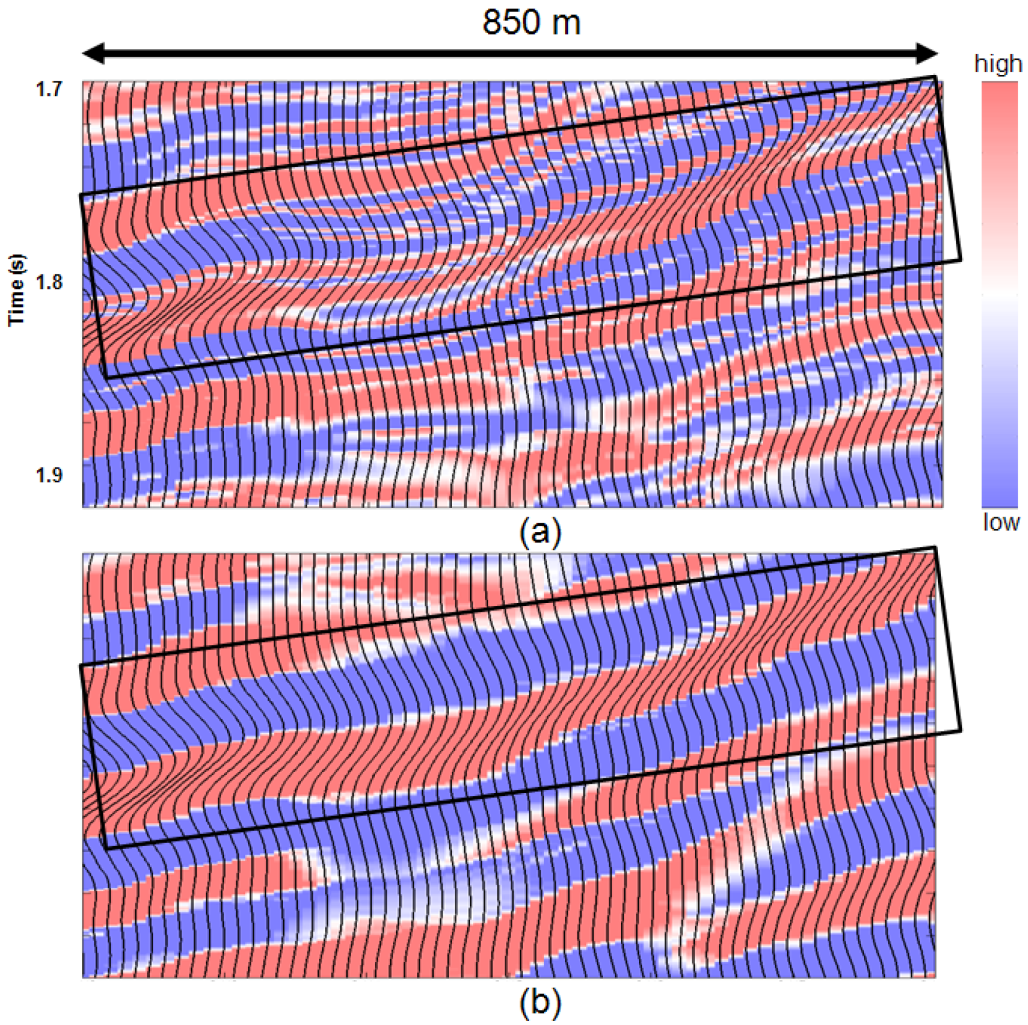

Figure 5.14: (a) BPI inverted impedance reveals many thin-bed layers within the rectangle. (b) SSI inverted data shows a low to high impedance transaction within the rectangle. The original seismic image data–overlayed as wiggles– shows one positive continuous amplitude that can be picked as a horizon within the rectangle.

clear on seismic image wiggles and not resolved using SSI. Black eclipse figures out a possible wedge structure in BPI which is not seen at both SSI or original seismic image wiggles.

Because of limited resolution, conventional SSI layers can be considered as the

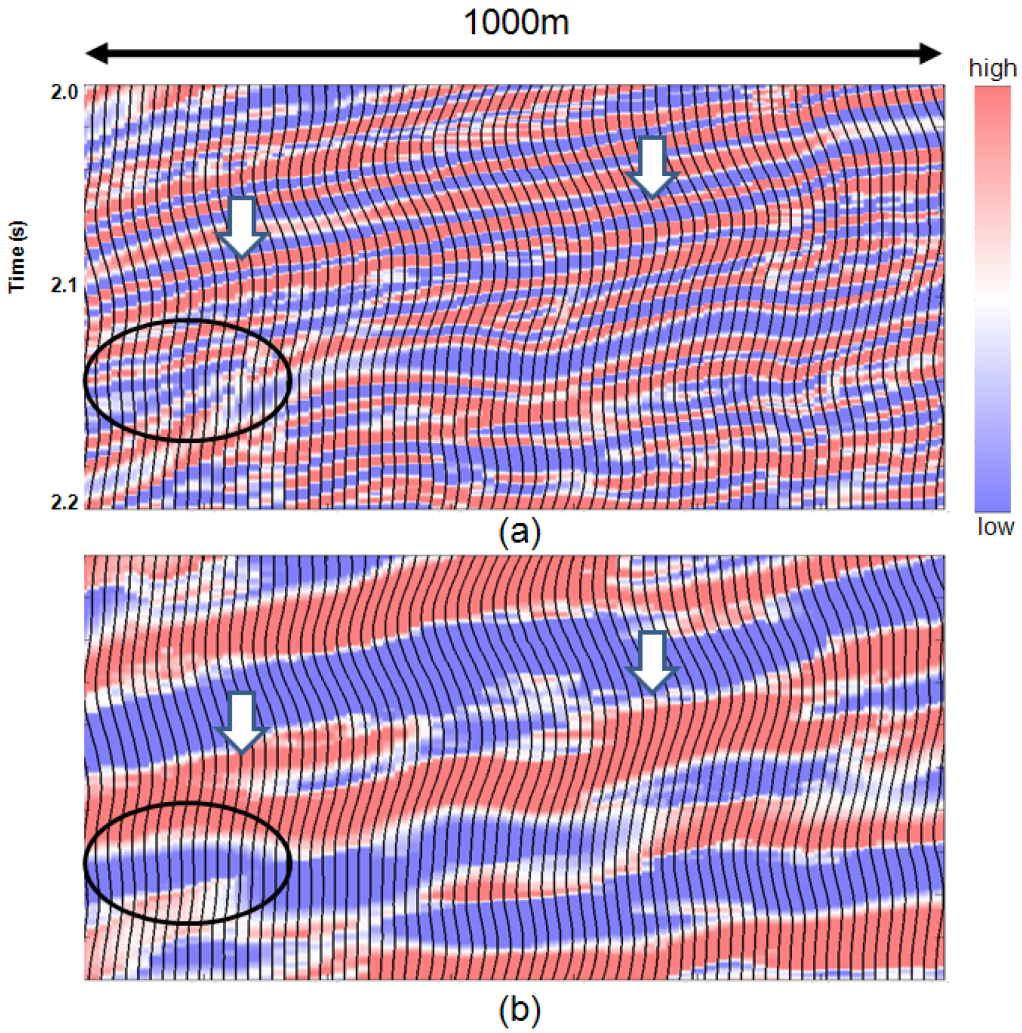

Figure 5.15: (a) BPI result reveals couples of lateral continuously updipping layering (white arrow) characteristic of undisturbed layer-cake geology. (b) SSI result shows a low and high impedance layering structure. Black eclipse in (a) emphasizes a wedge structure inverted by BPI that is unclear in the seismic image wiggles.

average of several thinner bed layers. Yellow rectangle in Figure 5.16 (a) reveals possible several thin bed layers, such as a low impedance thin bed embedded within a thick high impedance layer, or a high impedance embedded within a thick low impedance. SSI (Figure 5.16 (b)) resolves those thick layers as uniform layers. A possible pinch-out interpretation (black ellipse) shows up by basis pursuit inversion

in Figure 5.16 (a) which is not seen in sparse spike inversion.

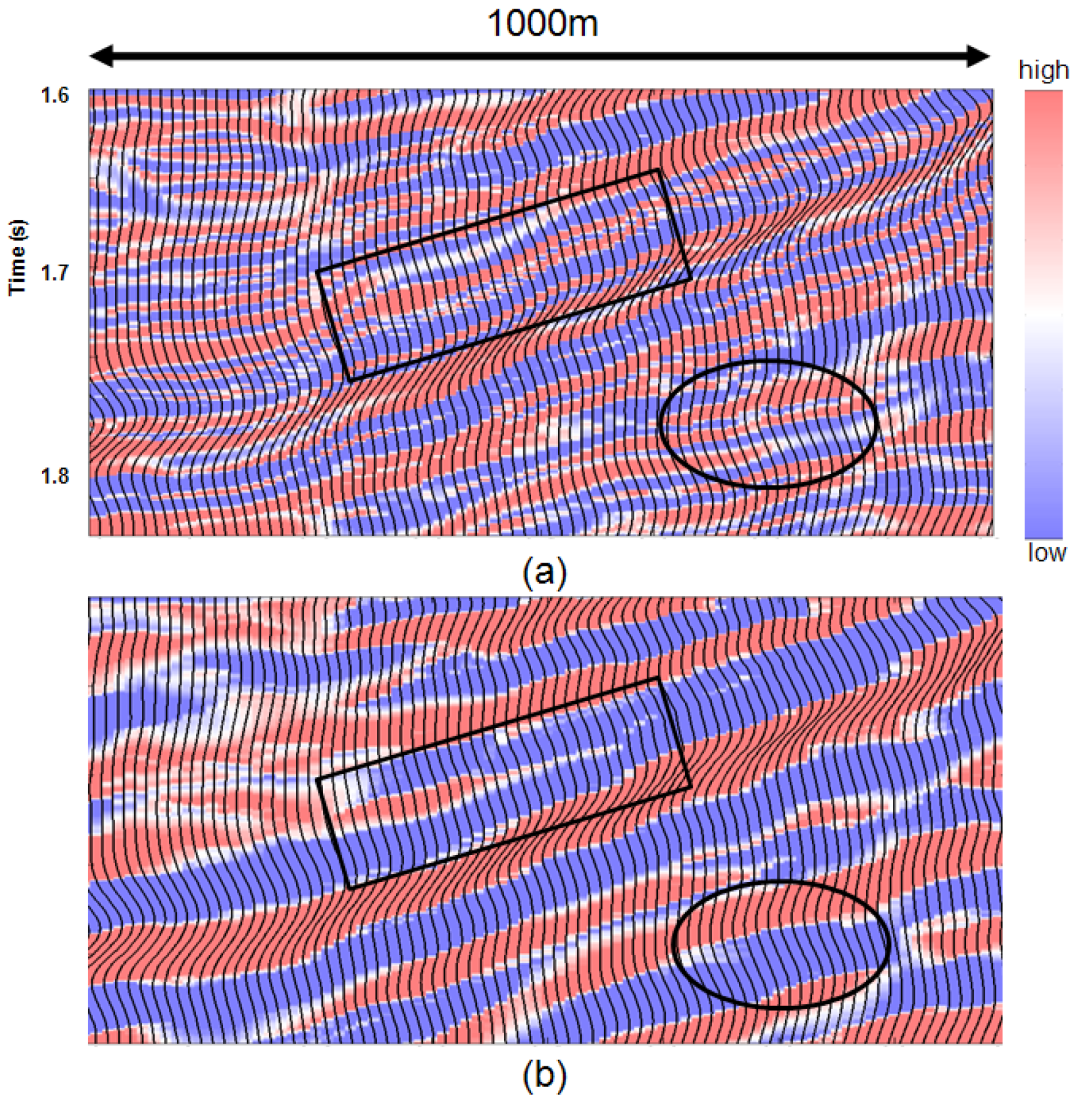

Figure 5.16: (a) the BPI result shows a continuous high impedance layer embedded in the low impedance within the rectangles while (b) SSI shows a pinch-out within the rectangle. Black ellipse shows a possible pinch-out structure in the BPI result that does not show up in the SSI results.

BPI (Figure 5.17 (a)) shows a possible channel (yellow circle) and fracture (white arrow) interpretation that is invisible using SSI (Figure 5.17 (b)). SSI merges the

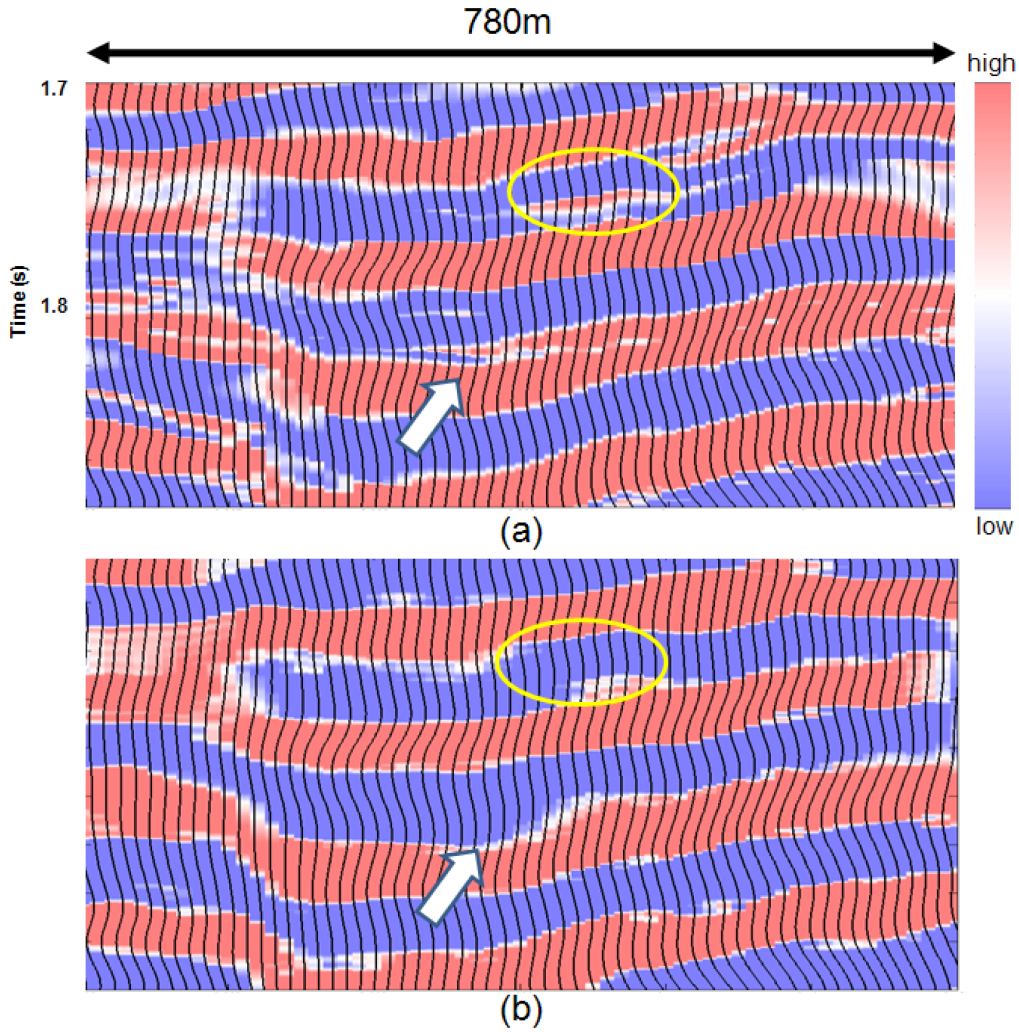

Figure 5.17: (a) BPI result shows a possible channel structure within the yellow ellipse; (b) SSI result does not show the channel structure. The white arrow in (a) points out a possible fracture that is invisible in the SSI result.

above structure below the resolution. However, there are still some clues detected unclearly by SSI. The basis pursuit inverted data shows a clearer picture of the channel geometry, with constant thinning of the channel-fill wedges toward the edges of the channel. In addition, the top and base bounding surfaces of the channel can be picked more precisely on the basis pursuit inverted data at the pointed area with less guesswork in the placement of horizons. Thus, BPI adds visual information that can

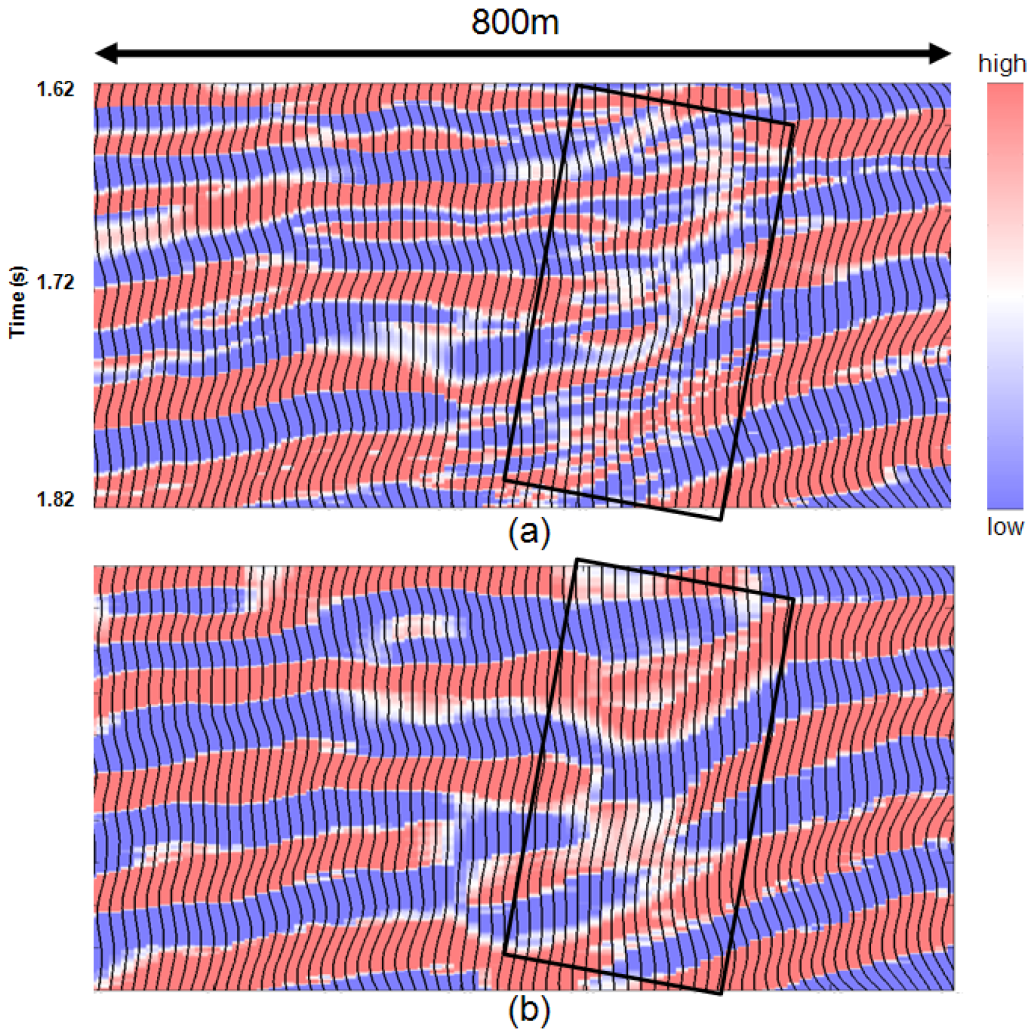

Figure 5.18: A fault is interpreted within the rectangle. (a) Fault related fractures within the rectangle show up with BPI. (b) The SSI result also shows up the discontinuity across the fault.

contribute to seismic interpretation by delineating geologic features of interest such as channels.

Figure 5.18 is an example of a fault structure. The original seismic wiggles, SSI and BPI results show a strong discontinuity cross fault. At the fault zone, BPI gives clear image of possible breaking fractures. Away from the fault, both sparse spike

and basis pursuit appear as similar structures, which means that the break images in rectangle Figure 5.18 (a) are probably caused by fault movements. We believe further investigation of this phenomenon would be very interesting.

5.4 Application IV

Figure 5.19 shows an example of 3-D data from the previous dataset. Such a 3-D application shows the impact of the inversion result for interpretation. The original seismic data is wavelet filtered earth, with much detailed subsurface filtered out. Figure 5.20 shows a reflectivity cube that highlights all the interfaces between layers which gives a framework of earth. Figure 5.21 shows a relative impedance cube that represents a detailed property of that earth. We show that relative impedance changes correspond to rock property changes permitting a great understanding of rock property.

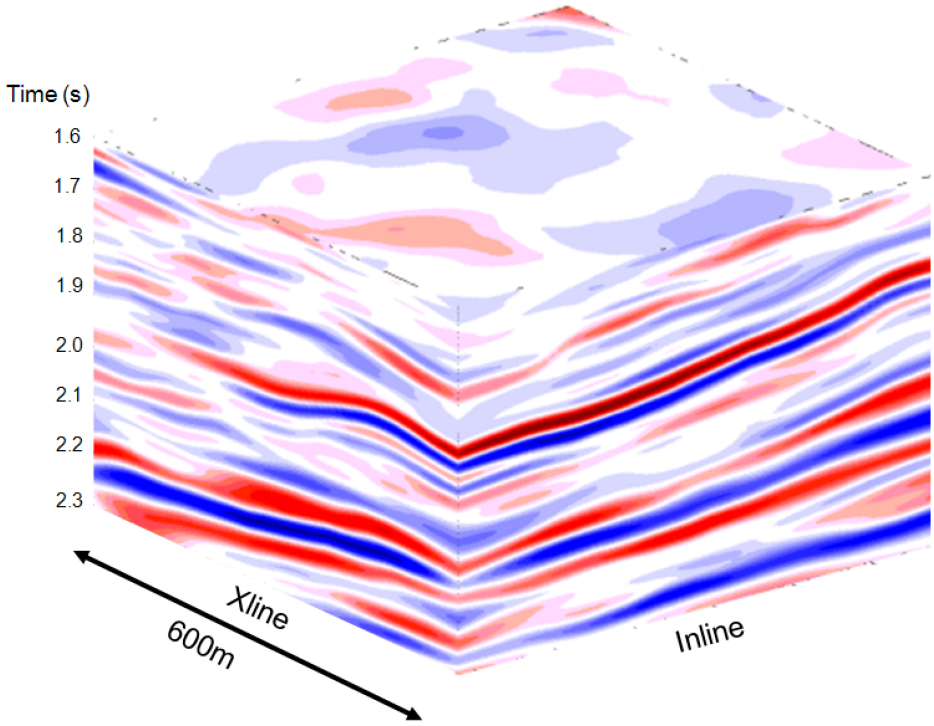

Figure 5.19: 3-D data set

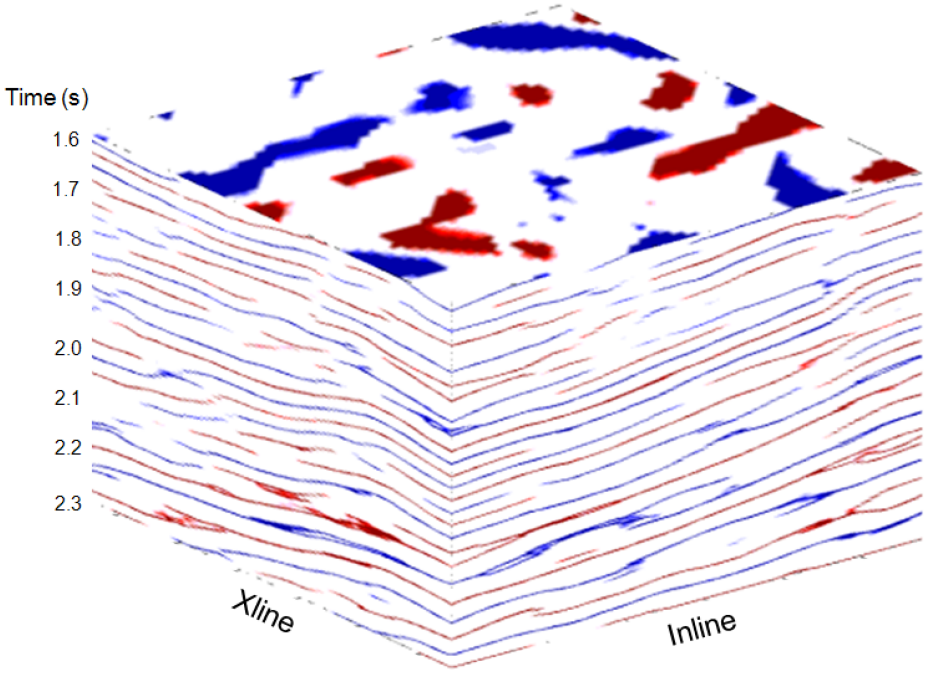

Figure 5.20: Inverted reflectivity from seismic in Figure 5.19

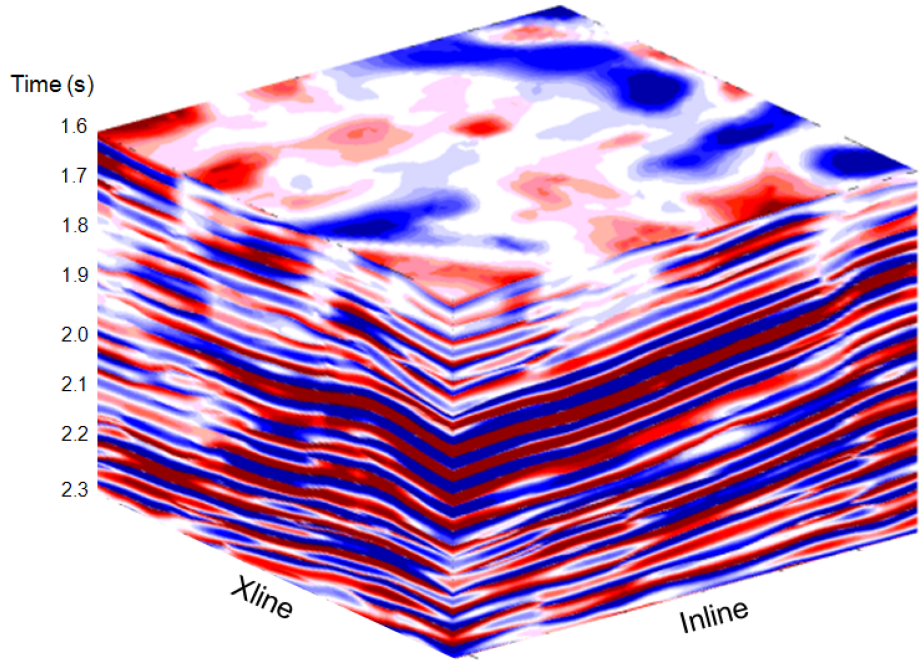

Figure 5.21: Inverted relative impedance

5.5 Application V

In this data application example, we show the impact of BPI on the 3-D data interpretation using three horizons. Figure 5.22 (a) shows the original seismic poststack image; its strong lateral discontinuity makes it very hard to interpret. In particular, the lateral discontinuity creates difficulty in picking the horizon. Superior vertical resolution and much better lateral continuity are achieved through use of BPI (as shown in Figure 5.22 (b)) making interpretation easier. By this result, it becomes much easy to interpret. Figure 5.22 (c) shows the Hampson-Russell model based inversion result. This result relies on the low frequency model to access the absolute impedance value. But, the Hampson-Russell inverted impedance is dominated by the low frequency profile, resulting in the lack of resolution.

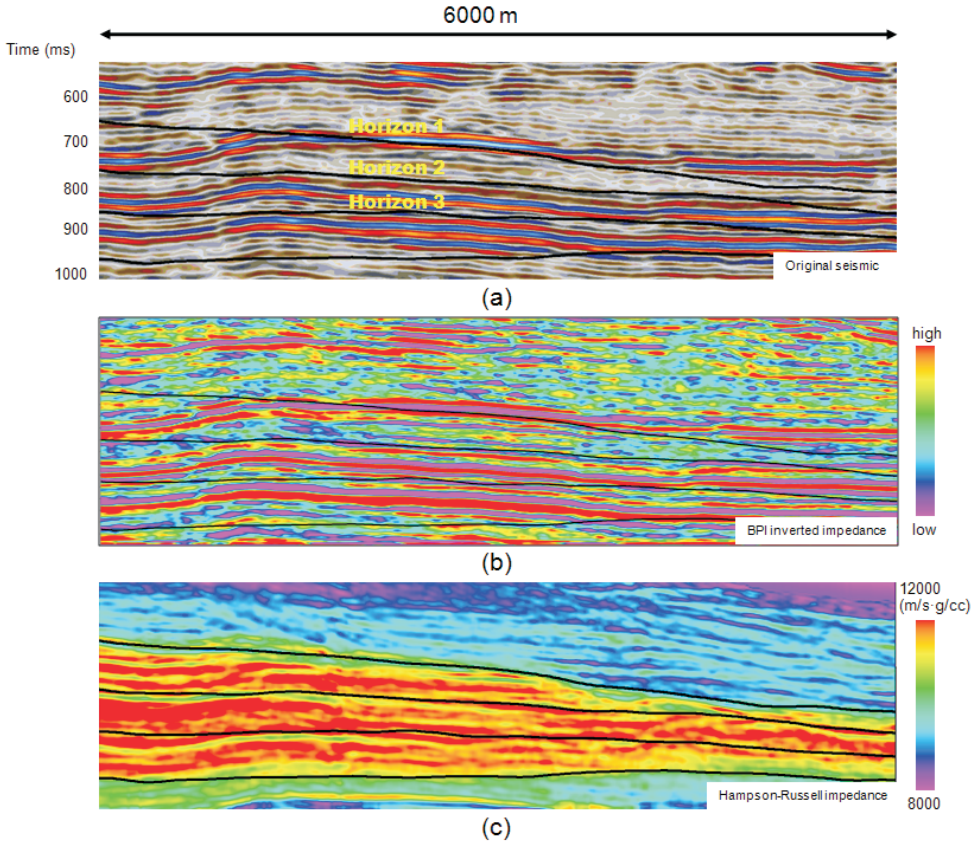

Figure 5.22: (a) Original poststack seismic image. (b) BPI result. (c) Hampson-Reusell inversion result.

Figure 5.23 shows three horizons map using BPI result and Hampson-Russell result. The BPI result reveals much more structures that than Hampson-Russell does.

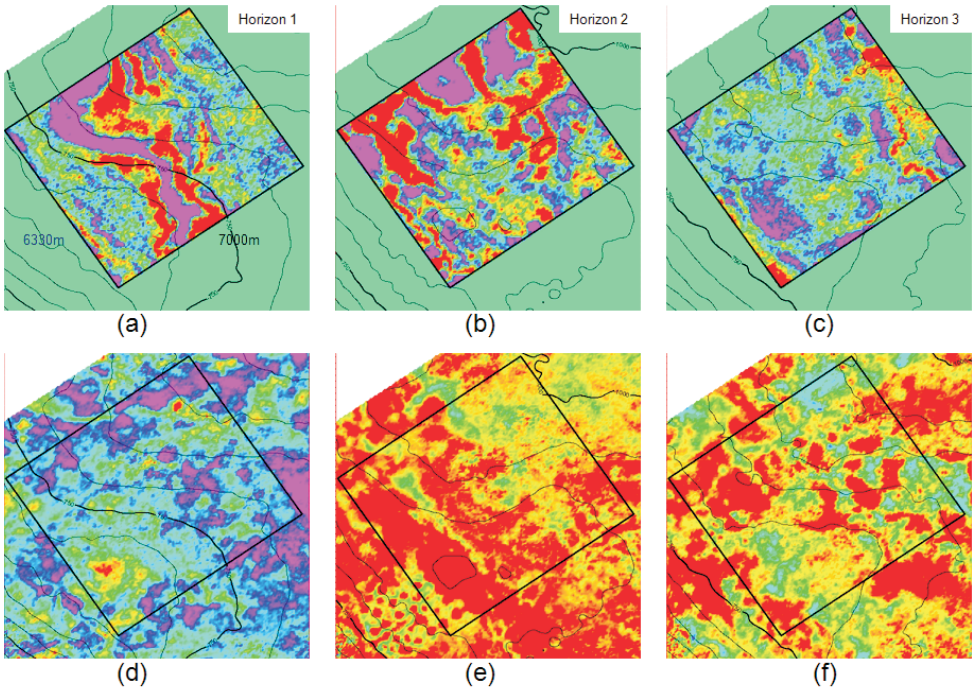

Figure 5.23: (a) and (d) show the horizon map of BPI and Hampson-Russell inverted results from Horizon 1. (b) and (e) show horizon map of BPI and Hampson-Russell inverted results from Horizon 2. (c) and (f) show horizon map of BPI and Hampson-Russell inverted results from Horizon 3.

5.6 Application VI

All previous applications demonstrate how BPI works on poststack image data. This application demonstrate that BPI works on prestack CDP gathers since prestack data also suffers from wavelet interference. Such interference is also caused by thin bed structures which makes it very difficult to pick separated velocity. BPI can increase the resolution of prestack data that can help separate hyperbolic events.

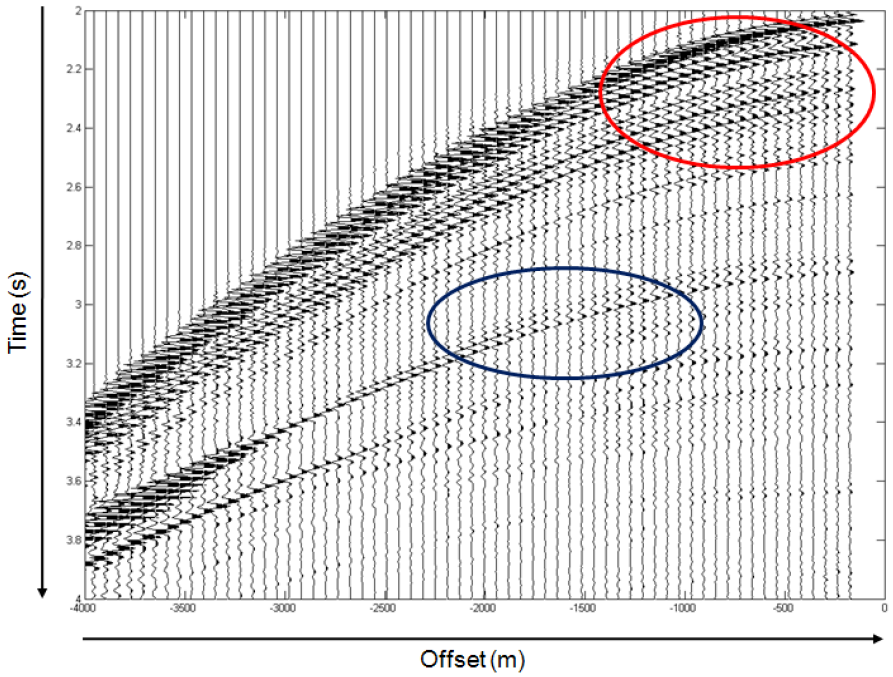

Figure 5.24: Original CDP gather. Red and blue ellipses show the possible interference caused by thin-bed layers.

Figure 5.24 shows a prestack CDP gather. Different hyperbolic curves are caused by velocity changes along a depth. But thin bed layer makes these curves interfered with each other, as shown in the red and blue ellipses, making it difficult to detect the velocity change. After BPI is applied, Figure 5.25 shows a high resolution reflection CDP gather. Figure 5.26 shows the detail comparison between the original prestack CDP gather and the BPI inverted data that interfered hyperbolic events are separated. When applying velocity analysis on the BPI inverted gather, a high resolution velocity structure is approached. Figure 5.27 (a) shows a semblance section based on the original CDP gather. Except the first hyperbolic curve, which comes from the water bottom holding a constant velocity of 1500m/s at about 2 second, all the other events are distorted by interference. The two white ellipses point out the aliasing area that

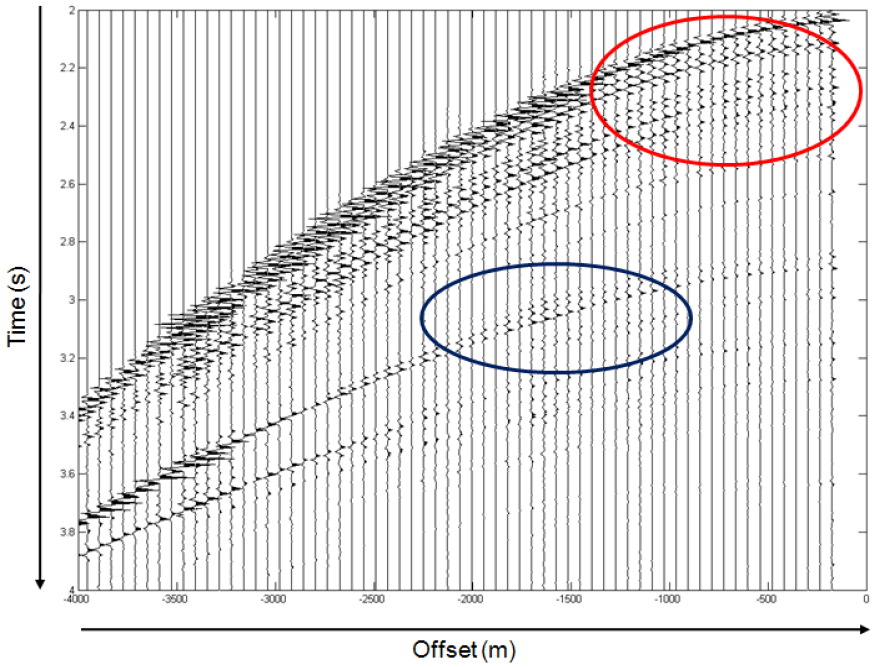

Figure 5.25: Inverted CDP gather.

probably leads to an incorrect velocity. Semblance calculated from the BPI result (shown in Figure 5.27) shows a much cleaner velocity structure with those events separated. Semblance energy holds a much better concentration by the use of BPI, making RMS velocity easily picked.

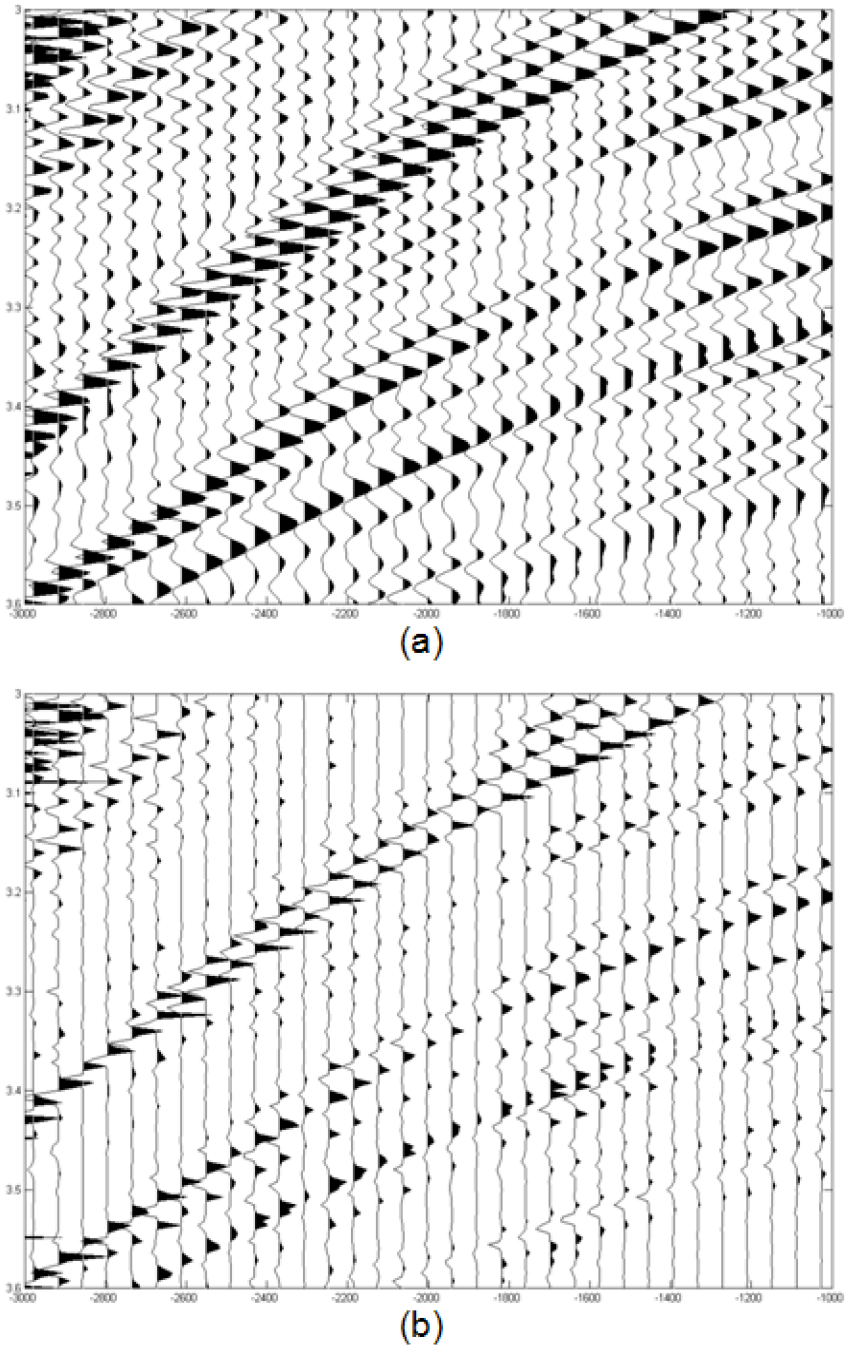

Figure 5.26: Detail comparison between original prestack CDP gather and BPI inverted data. (a) original CDP gather; (b) inverted CDP gather.

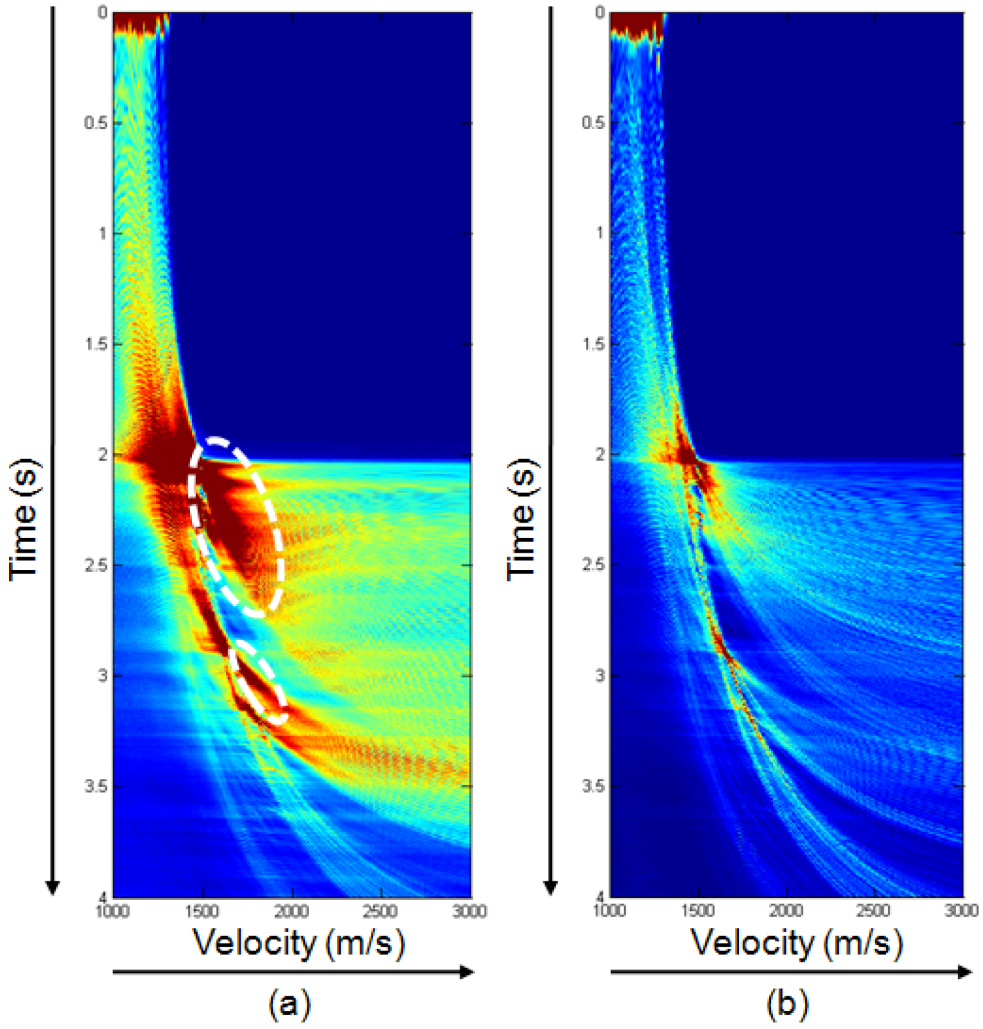

Figure 5.27: Comparison between semblance calculated from original and BPI inverted CDP gather. (a)Semblance calculated from original CDP has low resolution; (b) semblance calculated from inverted CDP has much higher resolution. Aliasing in (a) (white ellipse) is caused by the waveform interference can lead to wrong picking.

Chapter 6

Conclusions

The BPI method we describe here is a novel way of removing the wavelet from the seismic data and extracting a high resolution reflectivity. Although appreciable noise in the data deteriorates the performance of the inversion outside the frequency band of the original seismic data, BPI still enhances high frequencies beyond the bandwidth without amplifying noise. Nevertheless, the highly resolved seismic data retrieved in the form of reflectivity data are very useful for making accurate interpretations and prove to be advantageous in many ways, as we demonstrate using examples. A fundamental aspect of signal processing is that a valid signal cannot be produced by digital filtering at frequencies where the signal is absent. All an inverse filter can do is amplify noise where there is no or little signal. On the other hand, inverted seismic data commonly have frequencies outside the band of the original data. All spiky reflectivity inversions have frequency content that exceeds the original seismic bandwidth. We know that frequencies outside the original bandwidth of the data are within the null space of the inversion. The inversion process can put anything there;

the original seismic data will be recovered when the output spike series is convolved with the original seismic wavelet used in the inversion. So the issue is not whether one can output high frequencies that are not contained in the inversion. The issue is "how valid are they?" The answer depends entirely on the assumptions that are made (and the a *priori* information used to recover those frequencies), how well matched those assumptions are to reality, and how useful the results are. In our case, we only utilize the mild assumption that the earth is blocky, with a small number of reflections contributing to any given seismic reflection response. If there is an even component to these reflections, we utilize it to push resolution beyond the classical Widess limit. Clearly, there will be some cases where a blocky earth model is not appropriate, and the method will fail to some extent. Our conviction is that, more often than not, our assumption is a sufficiently reasonable representation of the earth and, data quality permitting, the inversion will produce useful results.

Beginning with a L_1 norm minimization least-square, combined with a wedge dictionary, BPI is used as a tool to unravel the complex interference patterns created by thin-bed reflectivity. These patterns can be inverted to obtain the original reflectivity. We developed and studied new analytical methods for BPI based on a wedge dictionary. Representing the seismogram as a superposition of a wedge dictionary constitutes a means of imposing on the inversion a *priori* assumption that sedimentary rocks occur as layers with discrete interfaces at the top and base which can be represented as such in a reflectivity series. When this assumption is valid, the consequence is that on the inverted results, there is geologically meaningful information at

frequencies outside the band of the original seismic image data. When this assumption is false, the recovered frequency information outside the band of the original seismic image data will also be false. For example, smooth impedance transitions may be inverted as blocky steps in impedance.

BPI with a wedge dictionary can be used to drive an inversion with significantly greater vertical resolution than that obtained by SSI, as tested by synthetic and field data. Field data also shows improved correlation to well logs and stratigraphic interpretation. These results are achieved without using well-log information as a starting model or as a constraint. The resulting inversion, therefore, is unbiased by preconceived ideas. As evidenced by the results of applying the method to real data, BPI has great potential as a practical tool for seismic exploration. For example, a prestack application offers great promise to improve velocity analysis.

The BPI we describe demonstrates improvement in vertical resolution; however, we did not use well-log information after the wavelet-removal step. It would be desirable to investigate the effectiveness of using well-log data to further improve vertical resolution of interbedded layers, or gradational changes within layers, that are not revealed by BPI alone. Another broad application may be found in the prestack data. To perform migration inversion simultaneously on CDP gathers would be a significant innovation for seismic exploration.